

# We are IntechOpen, the world's leading publisher of Open Access books Built by scientists, for scientists

6,900

Open access books available

186,000

International authors and editors

200M

Downloads

Our authors are among the

154

Countries delivered to

TOP 1%

most cited scientists

12.2%

Contributors from top 500 universities



WEB OF SCIENCE™

Selection of our books indexed in the Book Citation Index  
in Web of Science™ Core Collection (BKCI)

Interested in publishing with us?  
Contact [book.department@intechopen.com](mailto:book.department@intechopen.com)

Numbers displayed above are based on latest data collected.  
For more information visit [www.intechopen.com](http://www.intechopen.com)



---

# Particle Jetting Induced by the Impulsive Loadings

---

Kun Xue, Xiaoliang Shi, Kaiyuan Du and Haoran Cui

Additional information is available at the end of the chapter

<http://dx.doi.org/10.5772/intechopen.68795>

---

## Abstract

Particle rings/shells/cylinders dispersed by the radial impulsive loadings ranging from strong blast waves to moderate shock waves form a dual coherent jetting structure consisting of particle jets which have different dimensions. In both circumstances, the primary jets are found to initiate from the inner surface of particle layers and propagate through the thickness of particle layers, which are superimposed by a large number of much smaller secondary jets initiating from the outer surface of particle layers upon the reflection of the shock wave. This chapter first presents a summary of the experimental observations of the hierarchical particle jetting mainly via the cinematographic techniques, focusing on the characteristics of the primary particle jet structure. Due to the distinct behaviors of particles subjected to the strong blast and moderate shock waves, specifically solid-like and fluid-like responses, respectively, the explosive and shock-induced particle jetting should be attributed to distinct mechanisms. A dual particle jetting model from the perspective of continuum is proposed to account for the explosive-induced particle jetting. By contrast the shock-induced particle jetting arises from the localized particle shear flows around the inner surface of particle layers which result from the heterogeneous network of force chains.

**Keywords:** particle jetting, blast wave, shock wave, force chains, discrete element method, multiphase flows

---

## 1. Introduction

When particles are dispersed by an impulsive pressure loading, the expanding particle cloud typically forms a nonuniform structure that takes the form of particle jets whose leading edges are agglomerates of constituent grains [1–12]. A host of experimental evidence from a wide range of sources shows that the expanding cloud of explosively disseminated material comprises of

“particles” or fragments that have significantly different dimensions from those associated with the original material as shown in **Figure 1(a)** and **(b)** [1–7, 10–13]. Photographic evidence shows characteristic jets or fingers behind these expanding fragments. These coherent conical particle jets travel ballistically as shedding mass along the trajectories with increasingly diffuse edges.

Particle jetting has been widely observed in volcanic eruptions, supernovae, explosion of landmines, thermobaric explosion (TBX), fuel-air explosion (FAE), and dense inert metal explosive (DIME) [14–17]. The formation of particle jetting has also been observed during the impact of solid projectile on granular media [18]. The structure of particle jets in terms of the jet number or size is important to the viability of many applications. For instance, the strength of TBX and FAE needs to be enhanced by the after-burning of the reactive particles dispersed in the payload cloud. The detonation performance of the particle laden cloud depends on both the shape and concentration of the cloud which in turn is a result of the jet mixing [19]. In contrast with the large-scale injury radius of TBX and FAE, DIME utilizes the high-speed dense metal-particle jets to hit the targets in close range. Thus the momentum of particle jets determines the lethal radius. Another opposite application is mitigation of the blast pressure

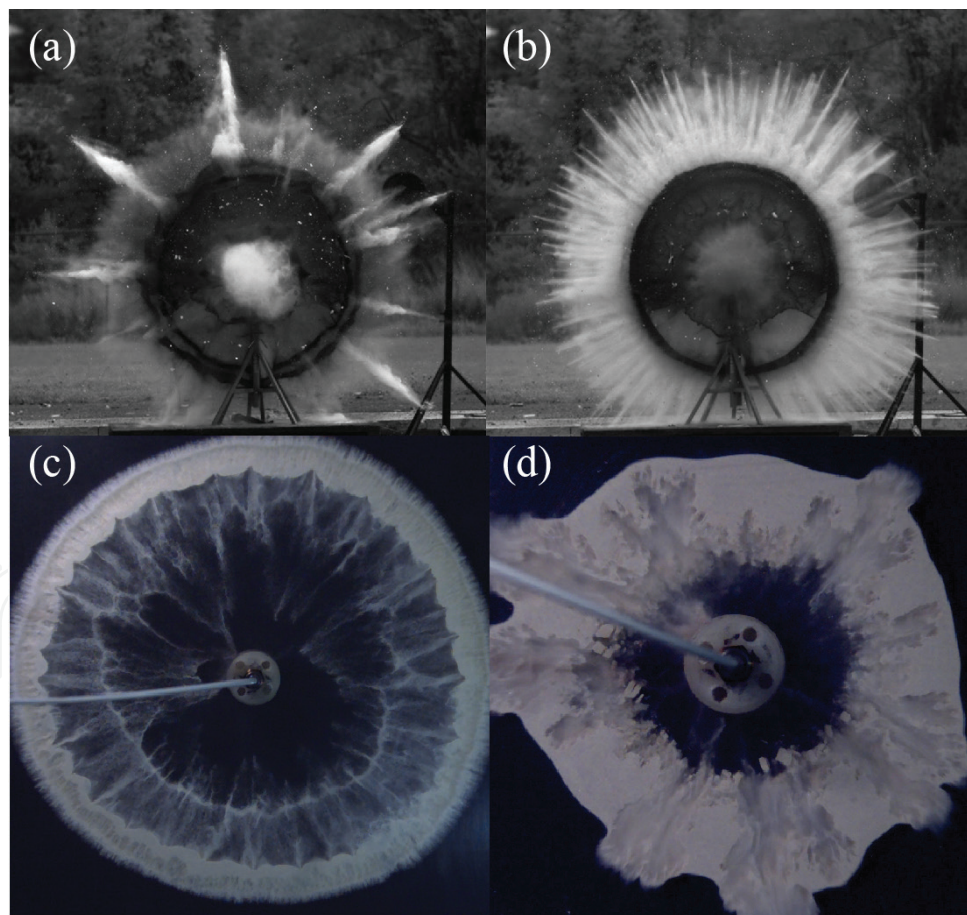


**Figure 1.** Explosive dispersal of dry (a) and wetted glass beads (b) using cylindrically stratified configurations [12]. Shock dispersal of flour (c) and quartz sand (d) particles using semi-two-dimensional configurations.

(both prompt and quasi-static) associated with the detonation, since a commonly used technique to reduce effects of blast from explosives is to surround the explosive with a layer of liquid, powder, or a slurry mixture of the two. Drag is seen as a potential mechanism to transfer energy from the blast wave to the disseminated particles or droplets so the size of particles or formation of jets is important in determining the efficiency of this mechanism. Frost and Zhang have reviewed many of the processes occurring in heterogeneous blast including jet formation [15, 17, 20, 21].

Extensive experimental investigations of the explosive- or shock-induced particle jetting mainly using cinematographic techniques provide fundamental data regarding both structure and evolution of particle jets. Closer look into the high-speed photos of either explosive- or shock-induced particle jetting reveals a dual structure (see **Figure 1(c)**) [1, 2, 12]. Primary jets initiated on the inner surface of the particle layers take shape during the first dozens of microseconds after the detonation of the central explosive evidenced by the light stripes detected from the radiographs of the explosive dispersal of particle shells [5, 6]. Upon the reflection of the shock wave on the outer surface of particle layers, a large number of smaller jets begin to burgeon from the outer surface and quickly develop into a full bloom [3]. The dominant primary jets are expelled from the outer surface and overtake the smaller secondary jets, merging of secondary jets occurring through the aerodynamic interaction. The respective evolutions of the primary and secondary jets are not so distinguishable from the radiographs and high-speed photos of the explosive dispersal of particles (see **Figure 2**). But the statistic distribution of jet size unravels two distinctive peaks representing the primary and secondary jets, respectively [13]. In order to overcome the difficulties in distinguishing the primary and secondary jets, a semi-two-dimensional configuration based on the Hele-Shaw cell that will be discussed in Section 3.1 was employed to access the evolution of both sets of jets subjected to the radial shock loading. Although the overpressure of weak shock waves is several orders of magnitude lower than that of blast waves, the formation and evolution of the primary and secondary jets as shown in **Figure 3** have astonishingly similar characteristics in terms of the initiation sequence and the signature structure [2]. Whereas whether or not the jetting process in these two extreme conditions follow the same path is still debatable.

Great efforts have been devoted to investigate the dependence of the jet number on a variety of parameters, including the configuration of charge, the mass ratio of the payload and the explosive (M/C), the inner and outer radius of particle layers, the particle material and size, and the moisture content, etc., mainly in the case of explosive dispersal of particles [2, 4, 6, 8, 13]. Specifically, Zhang et al. found that the numbers of primary and secondary jets dispersed by the 44 mm diameter of central explosive cylinder are 1.8 and 1.5 times those with the 10 mm diameter of explosive [14]. Frost et al. found that the jetting phenomenon is much more visible in cases of explosive dispersal of brittle or ductile powders, such as quartz sand, glass beads, SiC powders, aluminum powders, copper powders, compared with rigid and hard powders, like stain steel particles that are dispersed into the particle cloud rather than particle jets [10]. Frost and Xue both found that the addition of the interstitial water/oil significantly increases the jet number [12, 13].

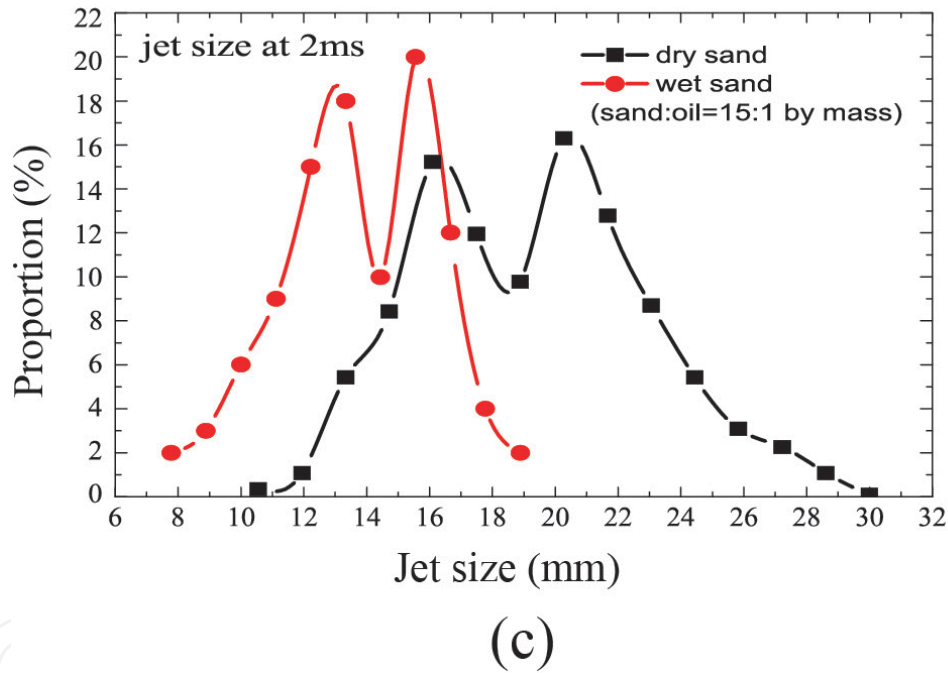
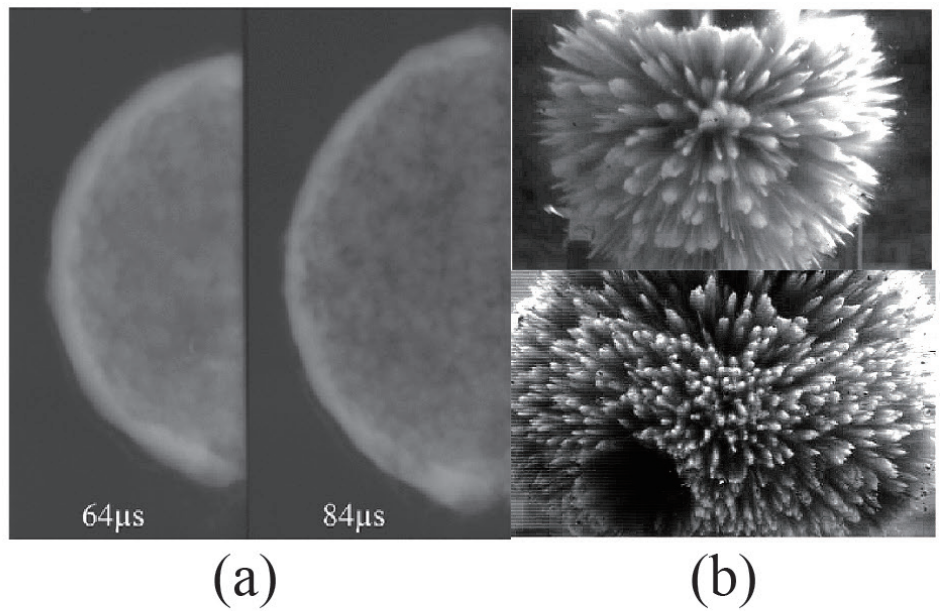
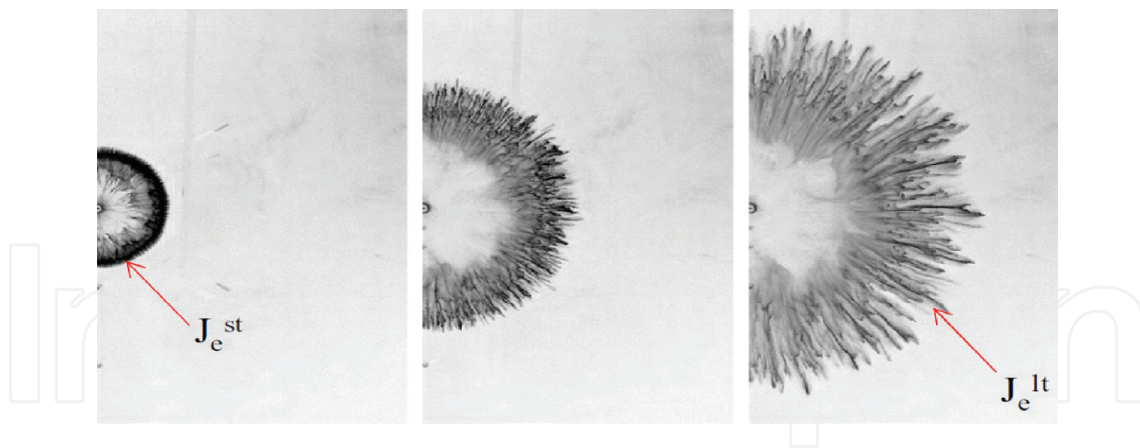


Figure 2. Radiographs and high-speed photos of explosive dispersal of glass beads (a) [5], dry (above panel of (b)) and wet (bottom panel of (b)) quartz sand grains [13]. (c): the statistic distribution of size of the explosive induced dry and wet sand jets at  $t = 2\text{ms}$  [13].

Some fundamental problems need to be addressed in this regard. First, several variables are correlated rather than independent so that it is impossible to single out the effect of the individual variable. For instance, changing the inner or outer radius of the particle layers or particle materials would inevitably alter the M/C that proves to be key factor determining the jet number. Rodriguez et al. proposed an alternative way to measure the effects of pertinent factors [2]. Acceleration of the outer surface of particle ring, which is a function of a variety of parameters, is found to be key determining factor. Therefore, choosing some proper dynamic



**Figure 3.** High-speed photos of semi-two-dimensional shock-induced particle jetting [2].

variables instead of structural parameters may well provide a new perspective in this regard, but entailing a thorough understanding of the physics underlying the particle jetting.

Second, distinguishing the primary and secondary jets from the radiographs or high-speed photos of the explosive dispersal of particles using either spherical or cylindrical stratified configurations is so difficult if not impossible that the validity of the experimental results is questionable thanks to the superimposition of two sets of jets on the timescale of microseconds. Adopting a semi-two-dimensional configuration in which particle rings are dispersed by the radial propagating shock waves seems to be promising approach to this problem. Besides, no detonation product gases obscuring the particle jets and substantially prolonged duration of jets facilitate the observation of particle jetting. But to what extent the shock-induced particle jetting can mimic that driven by the central explosion is quite questionable taking into account that the overpressure of shock waves is several orders lower than that of blast waves.

Predicting the jet number entails the knowledge of the mechanisms governing the primary and secondary jets, respectively. Several theories have been put forward, but understanding the origin of particle jetting still remains a significant challenge [3, 8, 9, 13, 22, 23]. The timescale for the formation of primary jets predicted by the Rayleigh-Taylor instability is much slower than the experimental observation [6]. Another interface instability theory involves the perturbation on the inner and outer surfaces of the particle layers that act as the microjets precipitating the macrojets propagating into the bulk. Ripple et al. demonstrated the evolution of the initial perturbation (see **Figure 4**) into well-developed jets and argued that the casing fragments and other imperfections may provide the initial perturbation [3]. However, particle jetting occurs regardless of the presence of the inner and outer casings and shows similar structure. Certain intrinsic imperfections with the length scale similar to the jets should exist if this theory holds. An increasing number of investigators have focused their attention on the bulk fracture of powder bed. Frost et al. postulated that the breakup of a layer of particles at high strain rates was governed by a balance of expansion inertia effects tending to fracture the layer versus viscous dissipation that tends to maintain the stability of the layer [24]. Along this line, Xue et al. developed a theoretical model account for the instability onset of the expanding powder shell [13]. Milne et al. conjectured that the powder is explosively compacted into

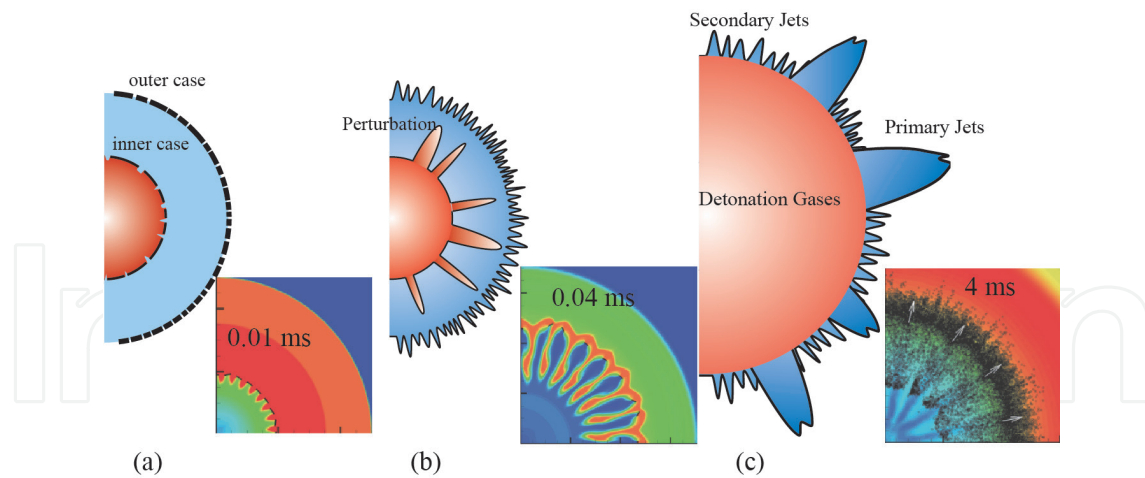


**Figure 4.** Schematics of the formation of primary and secondary jets caused by the inner and outer cases, respectively. (a): fragmentation of the inner and outer cases; (b): formation of primary and secondary jets arising from the gaps between fragments of inner and outer cases, respectively; (c): primary jets overtake the secondary jets. Inset: the corresponding snapshots from the hydrodynamic simulations of Ripley et al. [3,19].

a brittle solid which then forms cracks as the shell expands [5]. This conjecture is consistent with the observations that the primary jetting occurs during the first wave transit times. The major obstacle of this argument is that the compacted powder cannot sustain the tension or the surface energy, both among the essential components comprising the brittle fragmentation of solids. A few attempts try to understand the secondary jets, and the earlier works of Ripley et al. focused on the Richtmyer-Meshkov instability (RMI), which showed well-defined persistent jetting structures matching the number of prescribed outer surface perturbations [3]. However, the timescale for formation was slow and the surface instability did not propagate into the bulk [3]. Xue et al. modified the hollow sphere expansion model that originally accounts for the spallation of shocked solids so that the external particle jetting can be seen as parallel to the solid spallation [22].

Despite the resembling phenomenal features sheared by the explosive- and shock-induced particle jetting, the shock interaction with particles in the explosive dispersal is substantially stronger than that in the weak shock dispersal. In the former case, particles are compressed into solids with the density almost same as that of the constituent materials when the particle jetting commences. It suggests that a continuum approach is appropriate to model the explosion-driven particle jetting. By contrast, the weak shock wave only initiates the homogeneous or localized unsteady flows on the particle scale. The shocked particles behave more like fluids rather than solids. Unsteady and heterogeneous particle flows occurring during the weak shock interaction with particles entail a particle scale approach. Xue et al. described the particle scale formation and evolution of particle jets via the discrete element method (DEM), shedding some lights on the distinctive origins of the shock-induced particle jetting [25].

This chapter first reviews the up-to-date understanding of the phenomenology and physics of the particle jetting in both explosion-driven and shock-induced cases. Special attention is focused on theoretical progresses in unraveling the mechanism behind the respective

particle jetting and establishing models account for the onset of jetting, which is elaborated in Sections 2 and 3. Further work and possible breakthrough in this regard would be discussed in Section 4. The conclusion is presented in Section 5.

## 2. Explosion-driven particle jetting

### 2.1. Strong shock interaction with particles

One generally accepted fact of the explosive-driven particle jetting is that particle instabilities occur during the first dozens of the microseconds after the detonation of the central explosive. It is thus necessary to elucidate the interactions between particles, shock waves, and detonation product gases. Hydrodynamic simulations [22] have been performed to reveal the evolution of dry and saturated sand layers surrounding the spherical central explosive (TNT or HXM), the configuration illustrated in **Figure 5(a)**. In order to accurately describe the dynamic responses of wet sand with different degrees of saturation  $\beta$ , we adopted a modified version of Laine and Sandvik model developed by Grujicic et al. [26] to account for the effect of moisture content via explicitly incorporating the degree of saturation in the equation of state (EOS) and the strength model. Given the relative incompressibility of the water phase, the compressibility of the wet sand is increasingly reduced with the degree of saturation as illustrated by the EOS of the wet particles with varying saturation (see **Figure 5(b)**). Besides, the wet sand's yield stress is reduced due to the moisture-induced interparticle lubrication effects leading to a reduced effective friction coefficient (see **Figure 5(c)**). For details of the modified compaction model, readers can be referred to Refs. [26, 27] (see **Figure 6**).

The evolvement of the sand shell upon the blast wave can be well embodied by the variations in its radial density profile as shown in **Figure 3**. The sequence of events basically resembles those occurring in the shock-loaded water shell described by Milne et al. [5, 6]. When the shock front reflects upon the outer surface of the particle shell, the rarefaction wave travels back into particles and pulls away a thin spall layer moving forward into air. The compressive

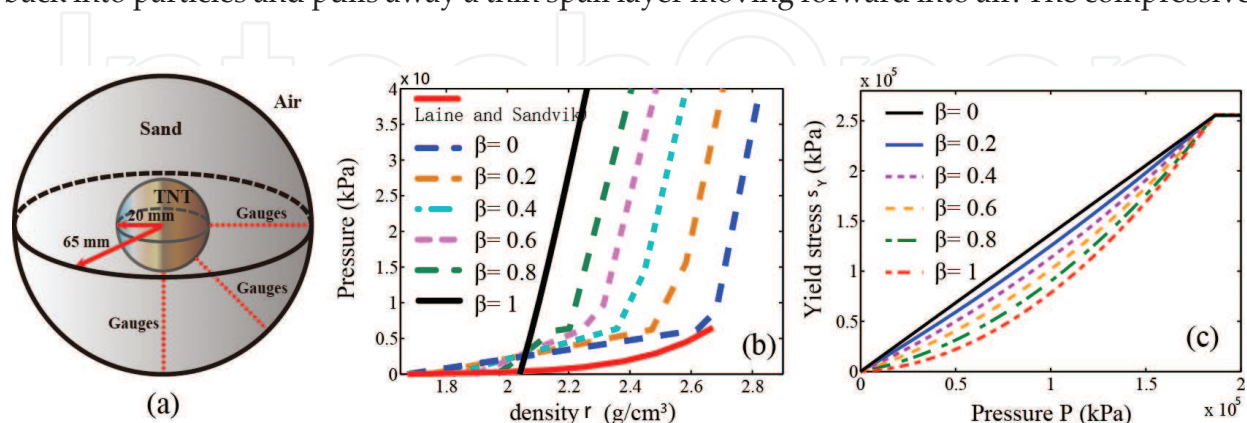


**Figure 5.** (a) Schematic of the spherical stratified configuration used in the hydrodynamic simulations. (b) EOS curves of the sand with varying degree of saturation. (c) Variations in dependence of the sand's yield stress on the pressure with increasing moisture contents [22].

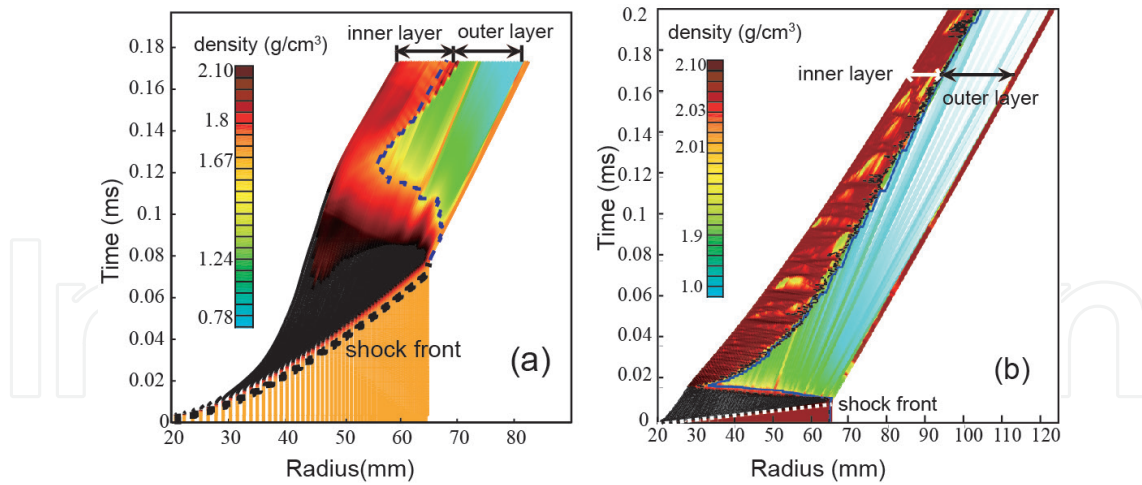


**Figure 6.** Evolutions of density profiles in dry sand (a) and saturated sand (b) after the detonation of the central explosive (TNT) [22].

stresses in the compacted particles are relaxed in the wake of the rarefaction wave accompanied by the rapid decrease of the packing density. The expansion of detonation product gases sends a shock wave into the particles, which arrests the rarefaction wave in its path in the case of dry sand or recompact particles diluted by rarefaction wave in the case of saturated sand. As a result, besides the outmost thin spall layer, the particle shell evolves into two distinct layers, namely the inner compact layer and outer dilute layers. The inner compact layer retains the maximum density almost as that of pure quartz and expands as an incompressible shell during a relatively long time, at least during the first hundred of microseconds after the detonation of central explosive. The hypothesis is supported by the consistent velocity across the thickness of the inner compact layer (see **Figure 7(a)** and **(b)**). Opposedly, particles inside the outer dilute layer lose the persistent contacts in the wake of the rarefaction wave. The

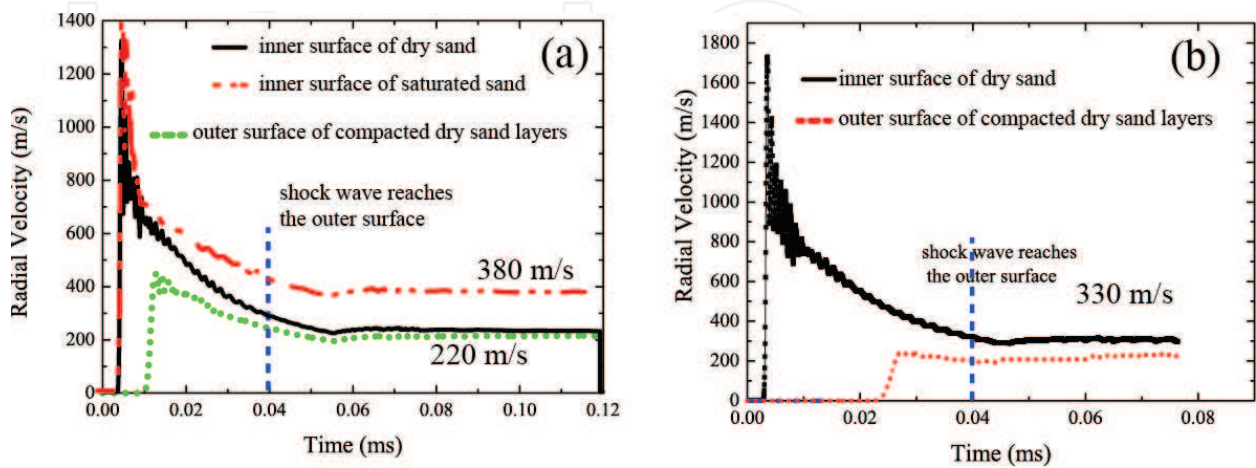


**Figure 7.** Evolutions of velocities of the inner and outer surfaces of the compact dry/saturated sand layer driven by the detonation of central TNT (a) and HXM (b).

mass ratio of the compact and dilute layers depends on the geometry and the composition of granular shell, as well as the strength of central explosive.

Due to the trivial compressibility of saturated sand, the acceleration of the compact saturated sand layer is much stronger than that of dry sand since less shock energy is dissipated among the compaction. The expanding velocity of the compact saturated sand layer is much larger than that of the dry sand (see **Figure 7(a)**).

## 2.2. Dual particle jetting model

The decomposition of the particle shell into the inner compact and outer dilute layers as a result of shock interaction prompts us to speculate that the fragmentation of the inner and outer layers correspond to the primary and secondary particle jetting, respectively. This speculation satisfies some fundamental facts that (1) the primary and secondary particle jets initiate from the inner and outer surface of particle shells, respectively; (2) the secondary particle jetting occurs upon the reflection of the shock wave on the outer surface; (3) the primary jets overtake the primary jets in later times. Therefore, a dual particle jetting model illustrated in **Figure 8** has been put forward to account for the formation of the primary and secondary jets. The following task is to elaborate the proper models describing the respective fragmentation of the inner and outer particle layers. These models should be based on the underlying mechanisms and validated against the experimental results, the onsets of primary/secondary

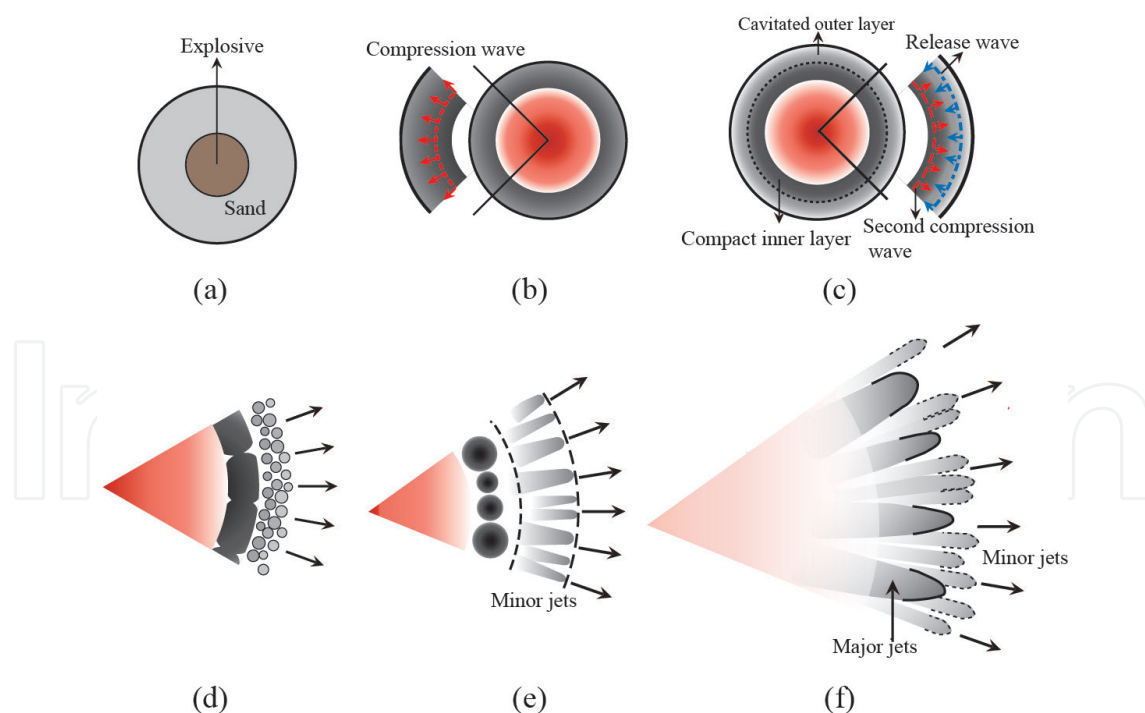


**Figure 8.** Illustration of the dual particle jetting model, which consists of the formation of the inner compact and outer dilute layers, and the breakup of these two distinct layers [22].(a):the initial annular configuration; (b): expansion of detonation gases issues the compression wave; (c): the reflected rarefaction wave causes the spallation of outermost layer; (d):fragmentation of the inner compact layer; (e): protrusion of secondary jets; (f): overtake of secondary jets by primary jets.

jetting, the size of primary/secondary jets, and the dependence of the jet number on a variety of factors as well.

### 2.3. Primary particle jetting model: the destabilization of the expanding shell

The consistent density and velocity across the thickness of the inner compact layer indicate that the compacted layer expands as the incompressible shell. Under this premise, we consider a sphere shell characterized by an inner radius  $R_1$  and outer radius  $R_2$  as shown in **Figure 9**, which can be determined by the hydrodynamic simulations (see **Figure 6**). The thickness of the shell is  $R_2 - R_1$ . Adopting the spherical coordinate system associated with the frame  $(e_r, e_\theta, e_\phi)$ , the outward divergent motion of the continuous sand shell demonstrated in experiments is modeled by applying a uniform velocity  $V_r e_r$  at the inner surface ( $R = R_1$ ), which can also be derived from the hydrodynamic simulation (see **Figure 7**).

Applying the continuity and momentum equations to the incompressible granular shells that can be described as viscoplastic materials, the analytical circumferential stress can be derived as follows (details of formulation can be referred to Ref. [13]).

$$\begin{aligned} \sigma_{\theta\theta} = & \frac{\rho V_r^2 R_1^4}{2} \left( \frac{1}{R^4} - \frac{1}{R_2^4} \right) + \frac{\eta V_r R_1^2}{\sqrt{2}} \left( \frac{1}{R^3} + \frac{2}{R_2^3} \right) \\ & - 2\rho(V_r^2 R_1 + A R_1^2) \left( \frac{1}{R} - \frac{1}{R_2} \right) + \sqrt{3} \tau_c \left( 2 \ln \frac{R}{R_2} + 1 \right), \end{aligned} \quad (1)$$

where  $\rho$  is the mass density of the sand shell,  $\tau_c$  is the yield stress, and  $\eta$  is dynamic viscosity. Bearing in mind that the yield stress,  $\tau_c$ , is a function of both saturation degree and the pressure applied on the inner surface which is in the order of  $O(10^0 - 10^1)$  Mpa (see **Figure 5(c)**), the yield stress of saturated sand ( $\sim 1$  MPa) is much lower than that of dry sand ( $\sim 13.7$  MPa) due to the lubrication effect assuming average pressure  $\bar{P} \sim 10$  MPa. The dynamic viscosity,  $\eta$ , is in the order of  $O(10^{-1})$ .

To predict the instability onset of the expanding sand shell, we will invoke a criterion for instability that has been shown to reasonably emulate more rigorous stability analysis [28]. This method can be viewed as an application of Le Chatelier's principle that states that for a system to be stable any deviation from equilibrium must bring about forces that tend to restore equilibrium. In general, the loss of stability is assumed to take place when an increment in strain occurs with no simultaneous increase in pressure or in load.

To obtain the circumferential pressure in the expanding shell, the circumferential stress from Eq. (1) is integrated through the thickness  $h$  of the shell,

$$\begin{aligned} T = & \int_{R_1}^{R_2} \sigma_{\theta\theta} dR \\ = & \frac{\rho V_r^2 R_1}{2} \left( \frac{1}{3} - \frac{4 R_1^3}{3 R_2^3} + \frac{R_1^4}{R_2^4} \right) + \eta V_r \sqrt{2} \left[ \frac{1}{4} + \frac{3 R_1^2}{4 R_2^2} - \frac{R_1^3}{R_2^3} \right] \\ & - 2\rho(V_r^2 R_1) \left( \ln \frac{R_2}{R_1} - 1 + \frac{R_1}{R_2} \right) + \sqrt{3} \tau_c R_1 \left( 1 - \frac{R_2}{R_1} - 2 \ln \frac{R_1}{R_2} \right). \end{aligned} \quad (2)$$

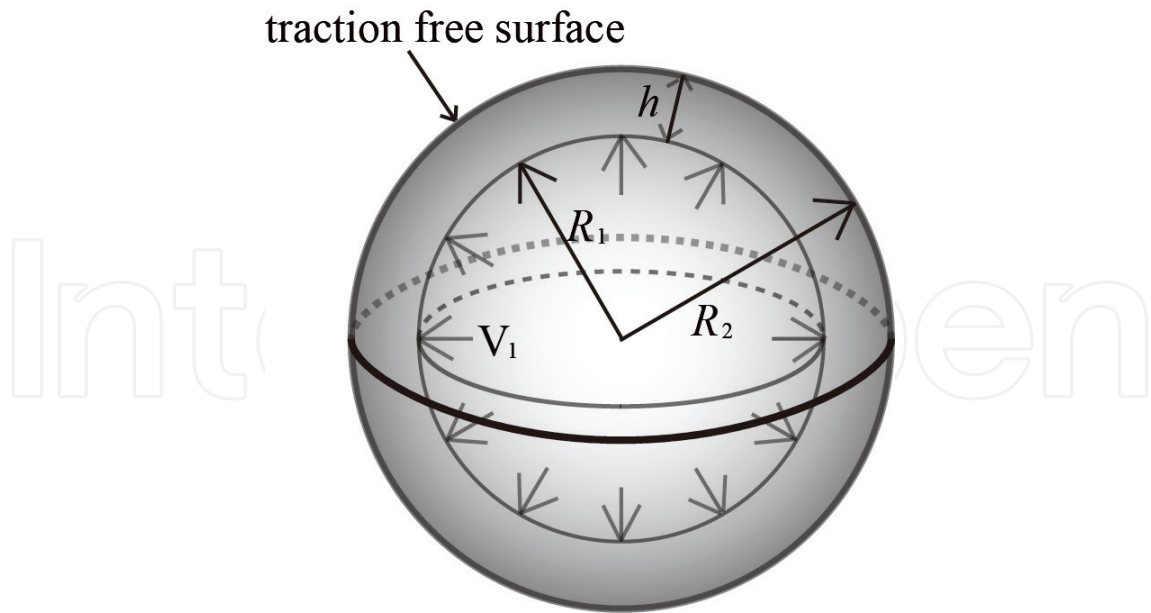


**Figure 9.** Configuration of an expanding spherical shell with inner radius  $R_1$  and outer radius  $R_2$  [13].

**Figure 10(a)** and **(b)** plot the variations of circumferential tension in dry and saturated sand shells with the expansion of the shell driven by the detonation of central TNT or HMX, respectively. The parameters are chosen as follows:  $\rho = 2.1 \times 10^3 \text{ kg/m}^3$ ,  $V_{r,dry,tnt} = 220 \text{ m/s}$ ,  $V_{r,dry,hmx} = 330 \text{ m/s}$ ,  $V_{r,saturated,tnt} = 380 \text{ m/s}$ ,  $V_{r,saturated,hmx} = 420 \text{ m/s}$ ,  $\tau_{c,dry} = 15 \text{ MPa}$ ,  $\tau_{c,saturated} = 0.5 \text{ MPa}$ . The terms with the coefficient involving  $\eta$  can reasonably be ignored as a result of the dimensional analysis. The instability onset is identified as the point at which  $dT/dR_2 = 0$ , beyond which the increase of strain does not render the corresponding increase of the pressure or loads. Specifically, the critical radius of dry and saturated sand shells corresponding to the destabilization onset driven by detonation of TNT or HMX are  $R_{c,dry,tnt} = 75 \text{ mm}$ ,  $R_{c,dry,hmx} = 80 \text{ mm}$ ,  $R_{c,saturated,tnt} = 98 \text{ mm}$ ,  $R_{c,saturated,hmx} = 105 \text{ mm}$ , respectively. Clearly, faster detonation velocity of explosive and addition of interstitial fluids can effectively delay the destabilization onset of the inner compact layer, equivalently the initiation of the primary jetting, consistent with the experimental observations. Likewise, we can predict the destabilization onsets of expanding sand shells with varying moisture contents as plotted in **Figure 11**, which agree well with those derived from the experimental observations. Note that the observed destabilization onsets of particle shells were determined from the high-speed photos that show the visible patterns in the surface of charge, which actually occurs after the destabilization onset.

The fragment size following breakup is substantially determined by the wavelength of the most unstable disturbance that has the greatest growth rate. Determination of a dominant unstable wave length is difficult due to the time-varying nature of the mean flow. Louis suggested that for a small value of  $\Gamma$ , the most disturbances are in a range of wavelengths between  $O(1)$  and  $O(1/\Gamma)$  times the instant thickness of the shell, where  $\Gamma$  is the dimensionless number as follows

$$\Gamma^2(t) = \frac{6\rho \bar{d}_{\theta\theta}^2(t) h^2(t)}{\tau_c}. \quad (3)$$

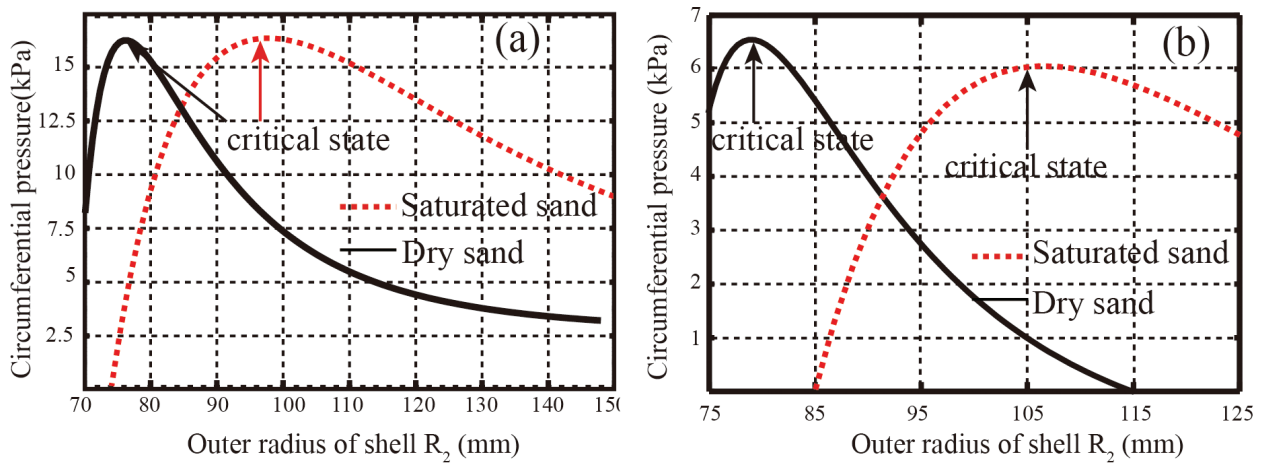


Figure 10. The variations of circumferential tension in dry and saturated sand shells with the expansion of the shell driven by the detonation of central TNT (a) or HMX (b).

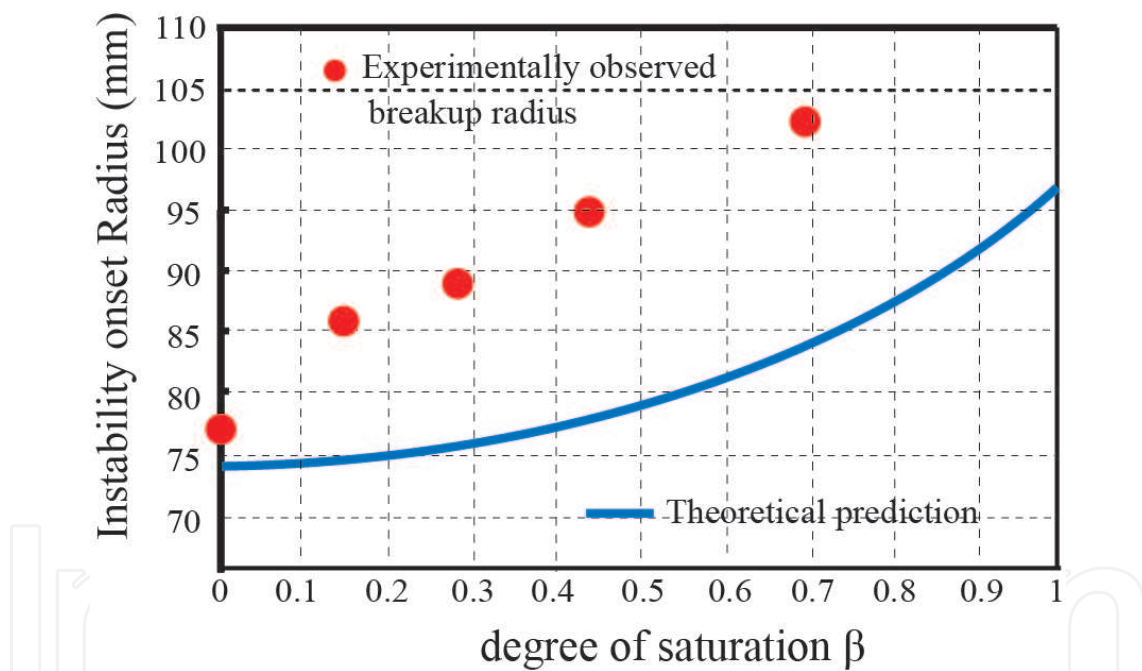


Figure 11. Theoretically predicted (curve line) and experimentally observed (red circles) critical radii of expanding sand shells with varying saturation degree driven by the detonation of central TNT.

In Eq. (3),  $\bar{a}_{\theta\theta}$  and  $h$  are average circumferential strain and the instant shell thickness, respectively. Along this line, we give the first order of the estimation of the range of fragment mass of dry sand shells, or equally jet mass  $m_{jet}$  as a function of the yield stress as shown in Figure 12. The experimental determined jet mass for the dry and moderately wetted sand falls well into the range predicted by the aforementioned model.

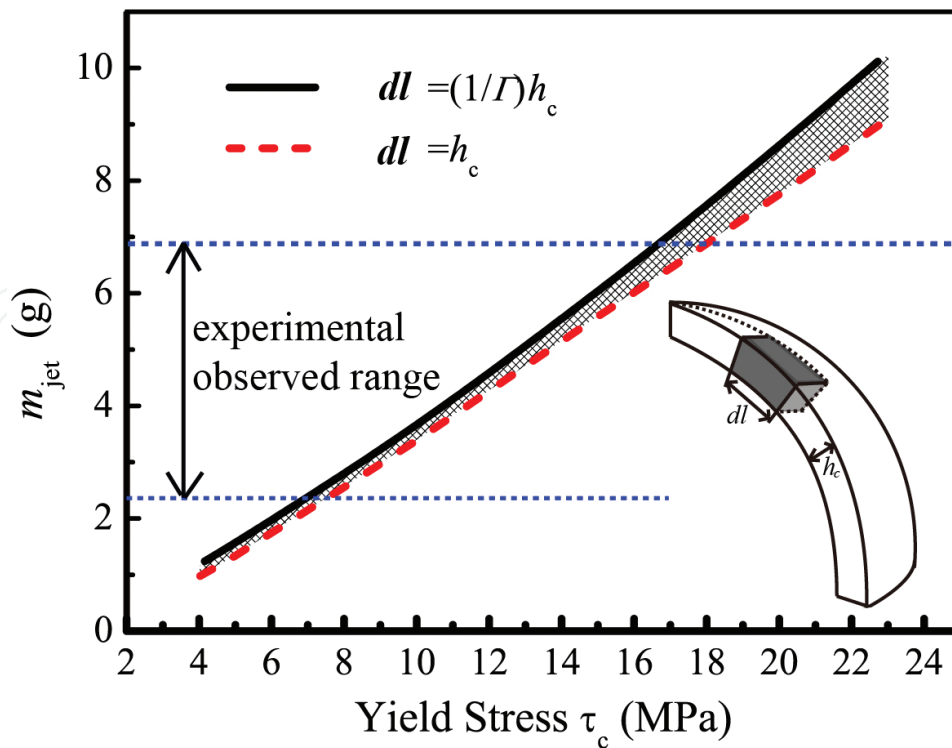


Figure 12. Primary jet mass vs. yield stress of sand shells [13].

#### 2.4. Secondary particle jetting model: cavitation model based on the expansion of hollow spheres

A micromechanical approach describing the cavitation process originally applied to ductile damage in solids has been proposed to account for the spallation in a liquid (or melt metal) subjected to a pulsed tensile load [29]. Xue et al. [22] adapted this cavitation-based spallation model to account for the disintegration of the outer particle layer, or equivalently, the formation of the secondary particle jetting, which is initiated by the unloading wave opposed to the tensile loading.

The incipient spallation of the outer particle layer takes the form of the macroscopic dilation in the wake of rarefaction waves. The dependence of the volumetric variation on the pressure is schematically plotted in **Figure 13(a)**. Within the frame of cavitation model, the bulk of the sample is seen as a collection of adjacent hollow spheres of internal and external radii  $a(t)$  and  $b(t)$  (see **Figure 13(b)**), respectively. The initial outer radius of the sphere  $b_0$  can be interpreted as the mean half-length between two neighboring nucleation sites as depicted in **Figure 13(b)**. As  $b_0$  defines the mass volume involved in the cavitation pattern, the “microscopic” pressure invoked by the cavitation varies with  $b_0$ . Since the “microscopic” pressure should agree with the “macroscopic” pressure dictated by the volumetric variation, this compatibility provides a criterion for the determination of  $b_0$ . To ensure the expansion of the microscopic hollow sphere is compatible with the dilation of the macroscopic outer particle layer, the microscopic expansion rate of the sphere,  $3b/b$ , should remain consistent

with the macroscopic dilation rate of the particle layer,  $\dot{V}/V$ , where  $V$  is the volume of the outer particle layer. The dilation rates at these two length scales are thereafter denoted by a single parameter  $D$ .

The spallation or, equally, the dilatation process of the outer layer consists of three stages. The first so-called hollow sphere expansion stage is prescribed by the relaxation of the accumulated pressure when the volumetric increase is dictated by the dilatation rate  $D$ . During the phase I, voids hardly begin to grow due to the inertial resistance. The end of the phase I of cavitation coincides with the full relaxation of the pressure marked by the restoration of the initial packing density. Afterward, the rapidly expanding matrix progressively becomes gaseous so that the particles interact by collision and the continuous displacement/stress field does not exist. Thus, the matrix and the void of the hollow sphere undergo the independent inertial expansion. The gaseous regime of the matrix is hereinafter denoted as the phase II of cavitation, which sustains as long as the matrix remains diluter than the initial packing state. Examining the packing density of the matrix in the dry sand suggests that the gaseous state of matrix maintains even when the fragmentation starts. By contrast, the gaseous saturated sand is soon transformed to the dense granular flows when the loose particles get recompressed

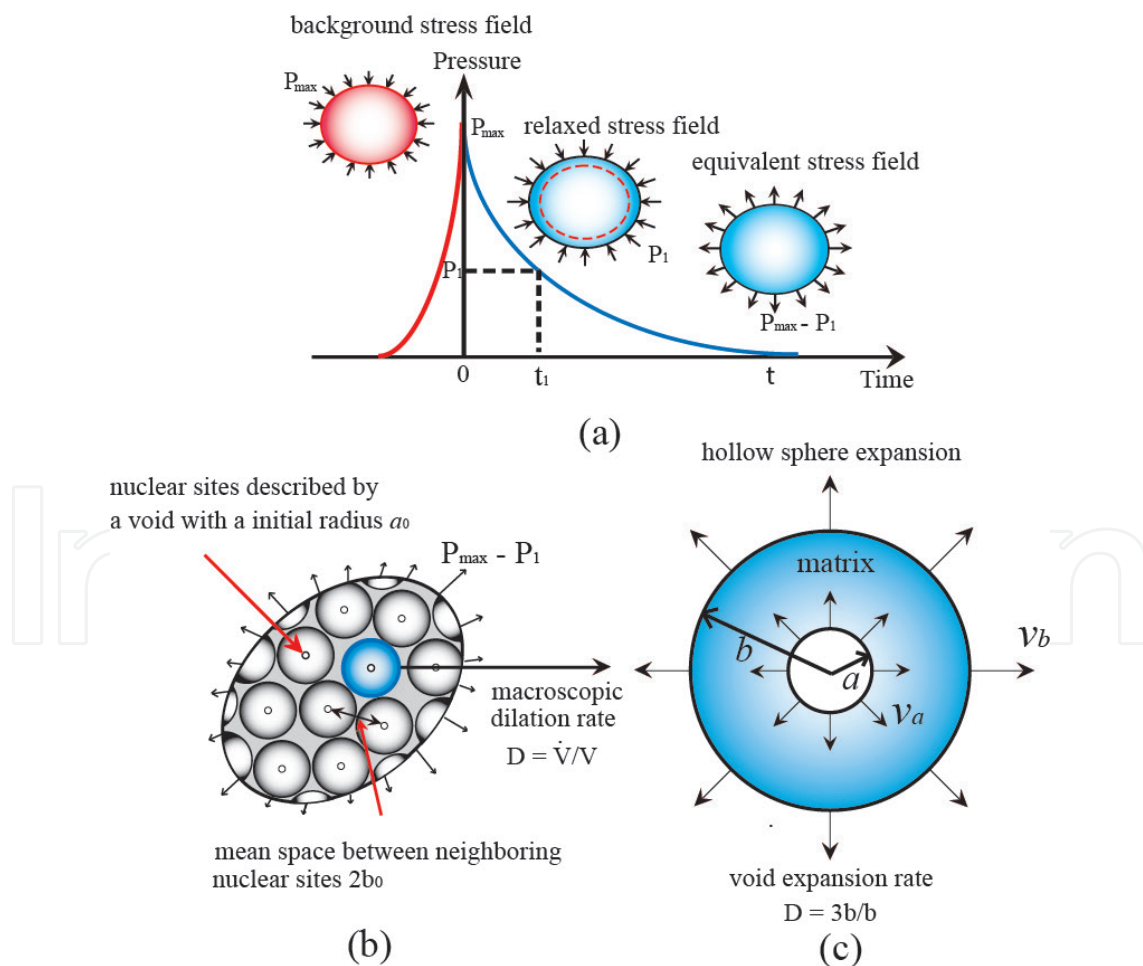


**Figure 13.** (a) Pressure relaxation experienced by the dry (dashed line) and saturated (solid line) particle layer accompanied by the dilation; (b) schematic of the hollow sphere pattern; (c) the expansion of the individual hollow sphere [22].

by the unconstrained outward expansion of the void. The subsequent expansion of the void, detonated as the phase III, is conditioned by the dense granular flow in the incompressible matrix.

Analytical modeling of these three sequent phases can be referred to Ref. [22]. This cavitation model estimates that the fragment size or equally the secondary jet size for dry and saturated sand ranges from 4 to 6 mm and 1.6 to 3.3 mm, respectively. Applying the proper fragmentation criterion, the predicted onset of secondary particle jetting occurs at 200–300  $\mu\text{s}$  for the dry sand and 50–100  $\mu\text{s}$  for the saturated sand after the detonation, respectively. The cavitation model is capable of predicting the fragmentation onset and the fragment size consistent with the experimental results. Therefore, cavitation is inferred here to be the most probable spallation mechanism of the outer particle layer.

The size of the secondary jets represented by twice the length between two activated nucleation sites,  $2b_0$ , is dictated by the compatibility of the “microscopic” and macroscopic pressures during the unloading of the compacted particles. Mathematically, smaller  $b_0$  in saturated sand is rendered by the significantly elevated dilation rate due to the larger elastic energy and faster moving release waves in the saturated sand. Micromechanically, it is the results of the competition between two neighboring cavities. Analogous to the scenario involving the Mott waves traveling between fractures (see **Figure 14(a)**), the expansion of cavity emanates the compressive waves into the neighborhood so as to suppress the potential cavitation nucleation in the encompassed area. The combined travel length of the compression waves emanating from the neighboring nucleation sites can be taken as the upper limit of the spacing between nucleation sites, namely  $2b_0$  (see **Figure 14(b)**). The unloading duration in saturated sand is almost one order shorter than that in dry sand, leading to the significantly shortened distance between two neighboring cavities.

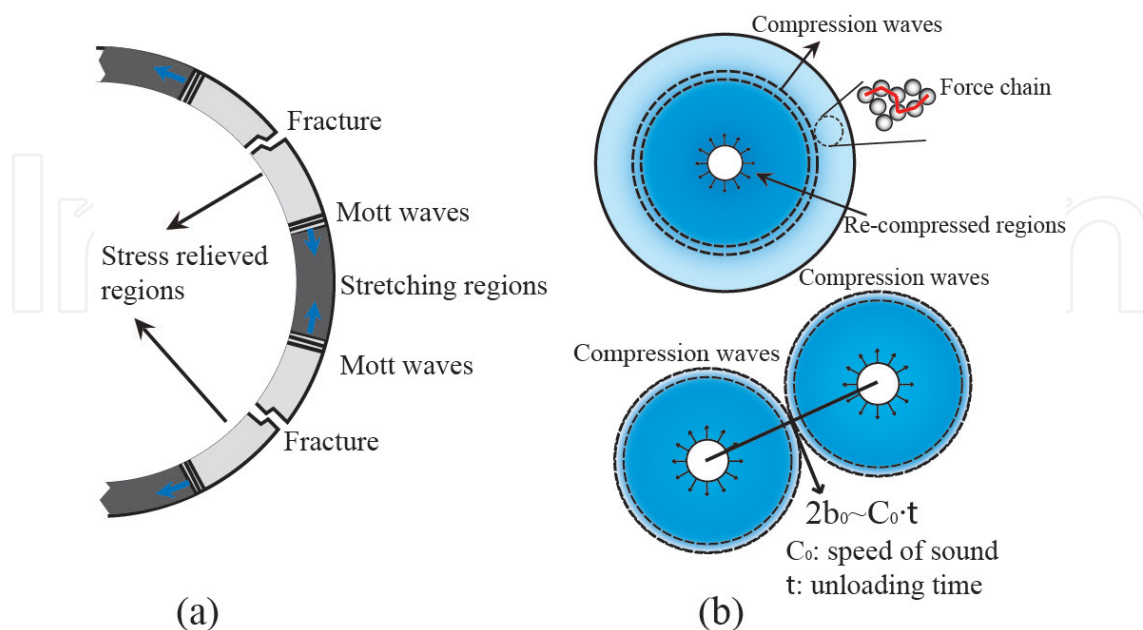


**Figure 14.** (a) A schematic of the Mott cylinder model with regard to the dynamic fragmentation of the solid cylinder (ring); (b) in particles, compression waves propagate away from an activated nucleation sites (above) retarding any activation of the nucleation sites within the travel radius and collide with those emanating from the adjacent nucleation sites [22].

### 3. Shock-induced particle jetting

#### 3.1. Quasi-two-dimensional particle jetting under moderate impulsive loads: phenomenal description

It is difficult to visualize the particle jet spread in the spherical or cylindrical experiments of the explosive-driven particle jetting due to the superimposition of jets, obscured by detonation gases, and the very short timescale as well. To overcome these disadvantages, Rodriguez et al. [1, 2] studied the particle jetting in quasi-two-dimensional configurations using moderate pressure loads induced by shock-tube-type facilities connected to a Hele-Shaw cell. With this convenient experimental setup, it is possible to conduct repetitive reliable experiments using a ring of particles in radial expansion trapped in a Hele-Shaw cell as shown in **Figure 15(a)**. More importantly, it is much easier to visualize and distinguish the primary and secondary jets. Xue et al. carried out the experiments of the shock-induced particle jetting using the apparatus similar to that devised by Rodriguez and reported similar observations of the particle jetting process.

**Figure 15(b)** shows the evolutions of dual particle jets of flour ring dispersed by the shock wave with the overpressure of 3.33 bar. The perturbation of the inner surface of ring can be detected at  $t = 1$  ms. The primary jets cutting through the inner surface are well defined in

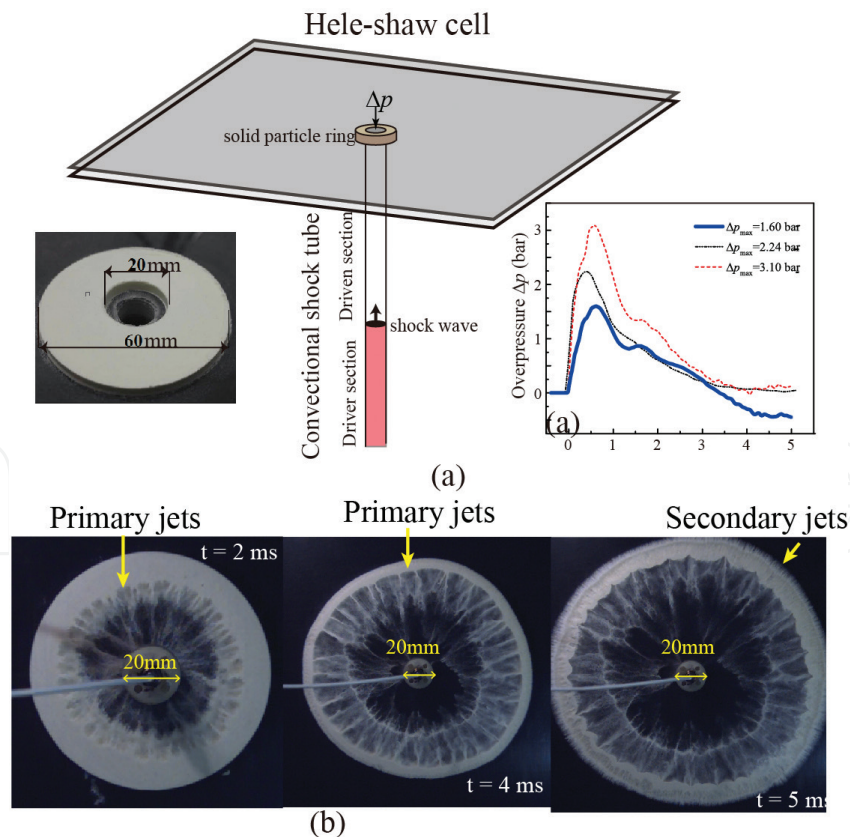


**Figure 15.** (a) Schematic of the quasi-two-dimensional experimental setup for shock induced particle jetting. Insets: photo of the four ring sample (left) and the overpressure histories at the exit of shock tube (right). (b) High speed photos of particle induced particle jetting.

the first several milliseconds. A large number of secondary jets burst out of the outer surface of ring 1.5 ms after the shock front reaches the outer surface. Afterward, the needle-like secondary jets undergo dramatic growth during the following one millisecond, while the tips of primary jets seem to be arrested at the bottom of secondary jets. It takes another several milliseconds that the primary jets overtake the secondary jets.

### 3.2. Particle-scale evolution of shock-induced particle jetting: DEM investigation

Experimental observations can only provide the configurational evolution of particle ring having no access to the particle-scale information, such as the particle velocities and forces. DEM has proven to be an effective tool to investigate the particle-scale velocity and stress fields in particles subjected to the static or dynamic loadings. Xue et al. performed the DEM simulations of the shock-induced particle jetting using the same geometrical configuration as in the experimental. Parametric studies were carried out to quantify the effect of a variety of variables, including the overpressure of shock loading ( $p_0$ ), the inner and outer radii of ring ( $R_{in}$  and  $R_{out}$ ), the packing density ( $\chi$ ), and particle size ( $d_p$ ). Details of the simulation can be found in Ref. [25].

**Figure 16** shows the shock dispersal of particle rings in terms of variations in velocity profiles. The shock-loaded particle rings with different initial parameters develop into the resembling jet structures with distinctive features as demonstrated in **Figure 16**. The formation and evolution of the primary jets in all cases, which are barely accurately described using experimental techniques, undergo two distinctive phases, namely the nucleation of the incipient jets and the competitive growth of the incipient jets. Here, the incipient jets are referred to as the localized shear flows or, equivalently, the fast moving particle clusters as shown in the innermost frame in each subfigure of **Figure 16**. The inner surface of ring remains smooth without visible dents or ripples so that the first phase is almost impossible to identify from the experimental observations.

The azimuthal velocity profiles of particle ring in early times shown in **Figure 17** demonstrate the nucleation of the incipient jets. No consistent pattern persists during the first millisecond, the spikes in the azimuthal velocity profile being transient and irregular. The flows behind the shock front are largely homogeneous around the perimeter. The following several milliseconds saw the dramatic transition of azimuthal velocity profile from irregular oscillations to regular fluctuations that are consistent throughout. This transition is clearly manifested by the substantial jump around  $t = 0.5\text{--}1$  ms in the variations of correlation coefficient of the two sequential azimuthal velocity profile (see **Figure 17(b)**). The peaks indicated in **Figure 17(a)** correspond to the localized shear flows, or equivalently the incipient jets identified in **Figure 17(d)**.

The radial growth of incipient jets in terms of the penetration depth into the bulk and the cross-sectional width is strongly uneven, the strong jets mushrooming outwards opposed to the retarded weak jets. As a result, the substantial elimination and the coalescence of weak jets prevail throughout the second phase. By contrast, the mushroom-like strong jet occasionally would split into multiple subjets, which is more likely to occur in rings with low packing density (see **Figure 16(c)** and **(d)**). Interestingly, the multiplication of strong jets can take place multiple times. The evolutionary characteristics of incipient jets revealed by the DEM simulations are substantiated by the experimental observations (see **Figure 18**).

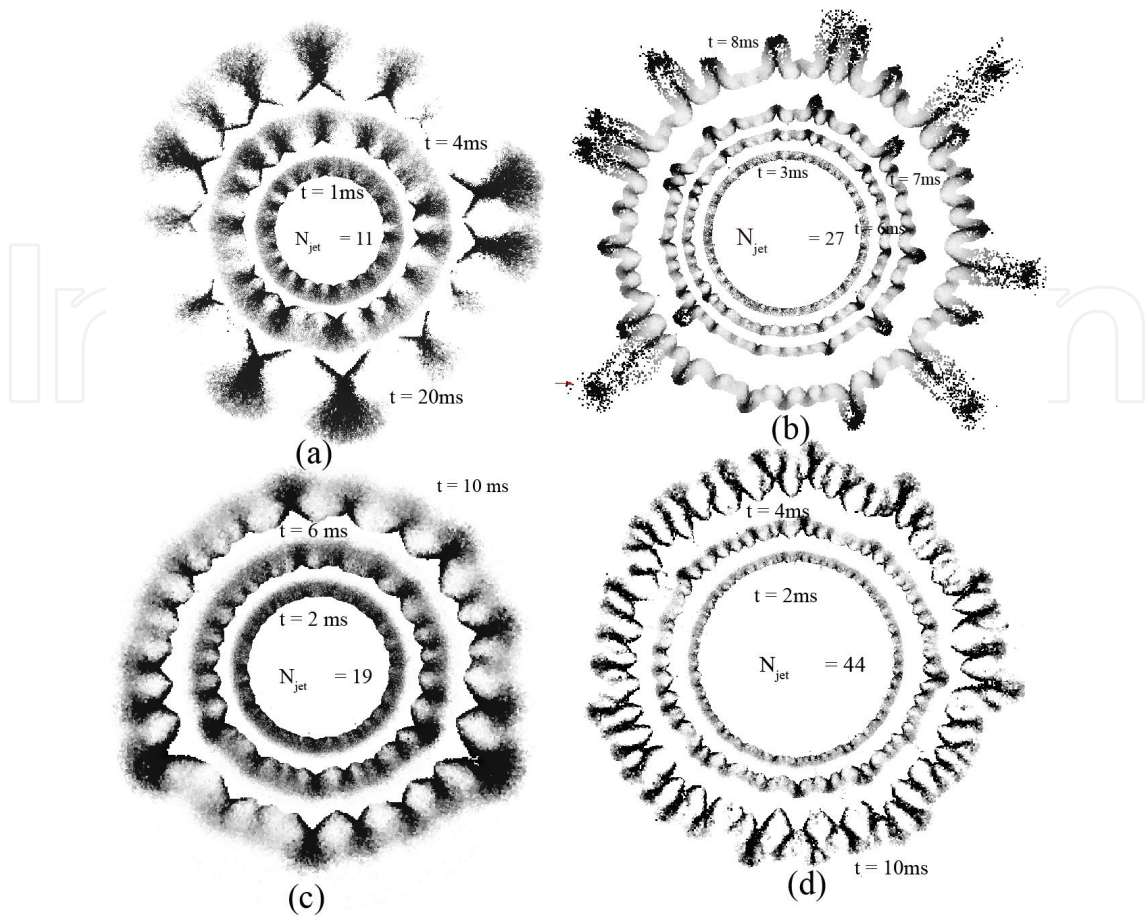


**Figure 16.** Evolutions of the velocity profiles in particle rings with different parameters. Particles are shaded according to the magnitude of velocities. (a)  $d_p = 2$  mm,  $p_0 = 5$  bar,  $R_m = 20$  cm,  $\chi = 0.55$ ; (b)  $d_p = 2$  mm,  $p_0 = 5$  bar,  $R_m = 35$  cm,  $\chi = 0.55$ ; (c)  $d_p = 2$  mm,  $p_0 = 5$  bar,  $R_m = 20$  cm,  $\chi = 0.42$ ; (d)  $d_p = 1$  mm,  $p_0 = 5$  bar,  $R_m = 20$  cm,  $\chi = 0.45$ .

The elimination of the weak jets significantly influences the temporal variations of the jet number as shown in **Figure 19**. After the chaotic initiation of incipient jets during the first several milliseconds evidenced by the strong oscillation of jet number, the jet number plummets dramatically in the following 5–10 ms. Afterward, the jet number undergoes much more gradual decrease until the jets are expelled from the outer surface of ring. Taking into account these fundamentals demonstrated in **Figure 19**, a physics-based equation as follows can be derived to describe the temporal variation of jet number,  $N_{jet}$ .

$$N_{jet} = N_{jet,i}(R_{in}, d_p, \chi) - V_{jet}(p_0, \chi)\Delta t(h, p_0, \chi). \quad (4)$$

In Eq. (4),  $N_{jet,i}$  represents the number of initial activated incipient jets;  $V_{jet}$  represents the decline rate of jet number during phase II (number per unit time);  $\Delta t$  is the duration of phase II. Surprisingly, the overpressure of shock waves does not have the discernible effect on the number of initial jet,  $N_{jet,i}$  which instead is a function of the inner radius of ring,  $R_{in}$ , the particle diameter,  $d_p$ , and the packing density,  $\chi$ . It suggests that  $N_{jet,i}$  is indicative of some intrinsic characteristics of particles, analogous to the intrinsic flaws of solids. The decline rate of jet number,  $V_{jet}$ , is clearly elevated by stronger shock loadings. Besides, lower packing density seems to hinder the elimination of jets. The duration of phase II,  $\Delta t$ , is among the most important factors governing the jet

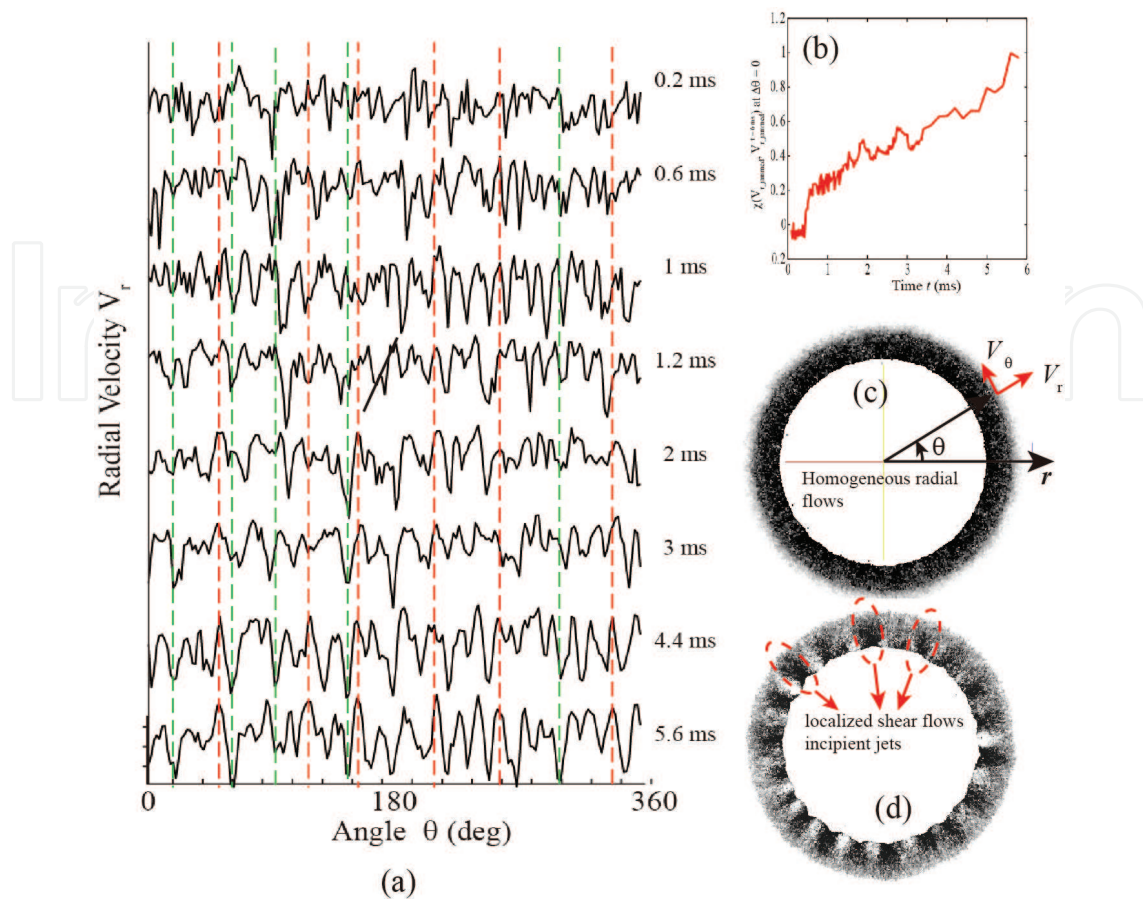


**Figure 17.** (a) Azimuthal velocity profiles of particle ring in early times and (b) variations of correlation coefficient of the two sequential azimuthal velocity profile of particle ring. Snapshots of particle ring at  $t = 0.2$  ms (c) and  $t = 3$  ms (d).

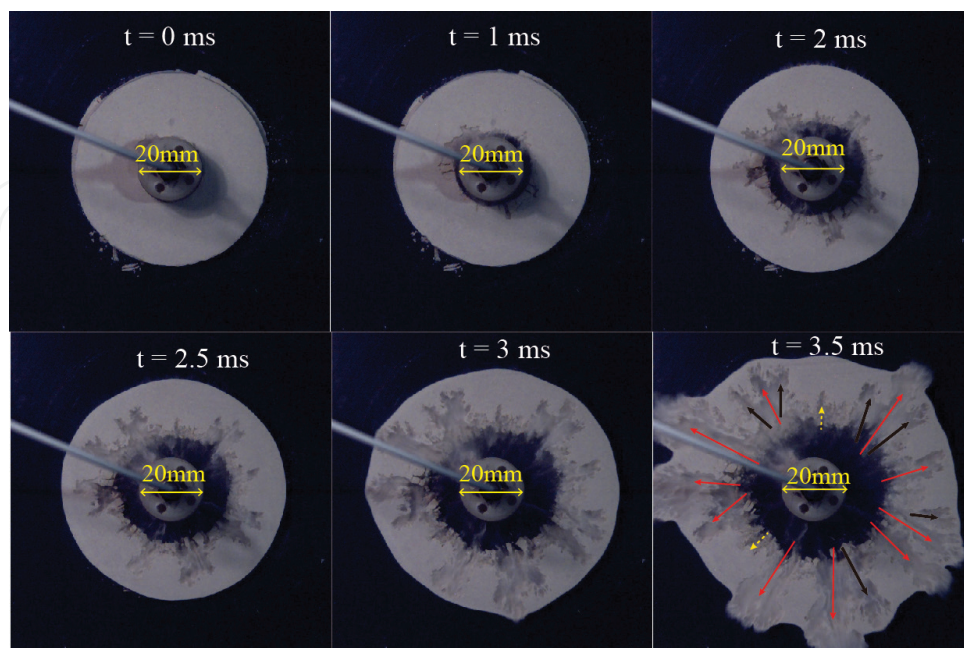


**Figure 18.** High speed photos of shock dispersal of corn quartz sand ring.

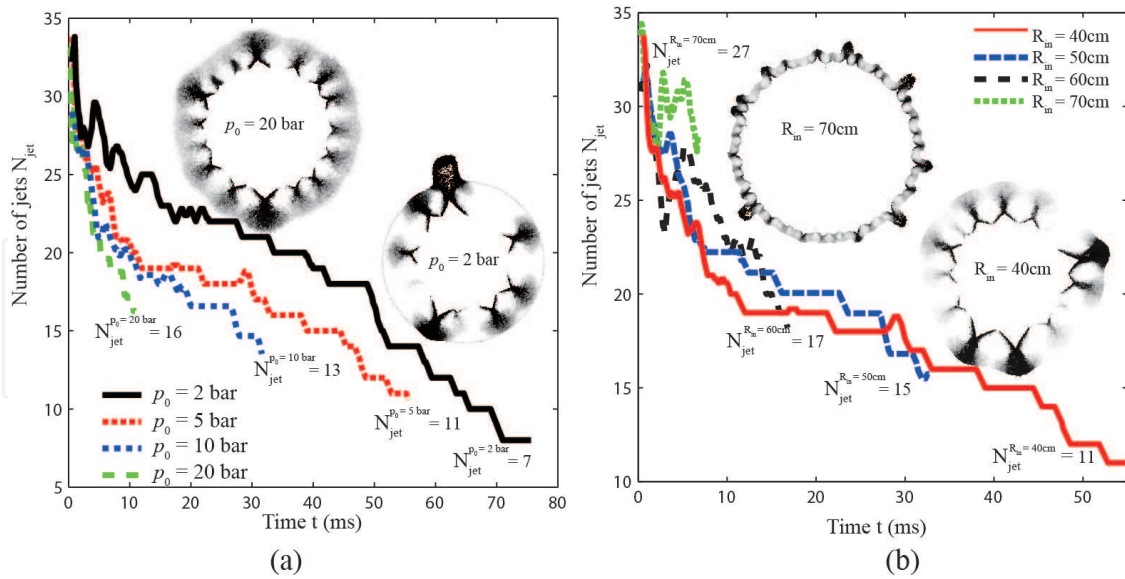


**Figure 19.** Temporal variations of the jet number with varying overpressure of shock loadings (a) and inner radius of ring (b). The inner radius of ring remains constant,  $R_{in} = 20$  cm in (a). The overpressure peak in (b) is 5 bar.

number, since the significant increase of jet number either due to the stronger shock loadings or larger inner radius of ring is dominantly caused by the truncated phase II. In another way, there is not enough time for the elimination of jets to fully unfold. The thickness of ring,  $h$ , the overpressure of shock loadings,  $p_0$ , and the packing density,  $\chi$ , are among the parameters influencing  $\Delta t$ .

### 3.3. Mechanisms governing the shock-induced particle jetting

The analytical formulation of Eq. (4) entails a thorough understanding of the underlying mechanisms, specifically the formation and elimination mechanisms of incipient jets. With regard to the formation of incipient jets, it is necessary to unlock the transition of the homogeneous flows to the localized shear flows. Unlike solids or liquids, the stress waves in particles travel through particle contact points and are primarily transmitted by the “force chains” that carry most of load in the granular materials [18, 30]. Meanwhile, the shock energy is dissipated by the random particle collisions. Because of the strong energy dissipation and nonlinear characteristics of granular systems, the inter-particle forces are transmitted through heterogeneous architecture of force chains such as shown in **Figure 20**, where the inter-particle contact forces are represented by inter-particle lines scaled with the magnitude of the contact forces. The initial contact network of particles (see the top panel in **Figure 20**) appears to be homogeneous in general with particle-scale heterogeneities. The cylindrical shock loading activates the contacts aligning with the local radial directions. Besides the intricate contact network in the innermost particle layers, a handful of long linear force chains extend radially from the inner surface toward the outer surface (shaded red in the second panel in **Figure 20**). These long linear force chains act as the arteries from which a growing number of short force chains are initiated, forming distinguishable clusters of force chains at  $t = 1$  ms with the dimensions much larger than that of constituent particles.

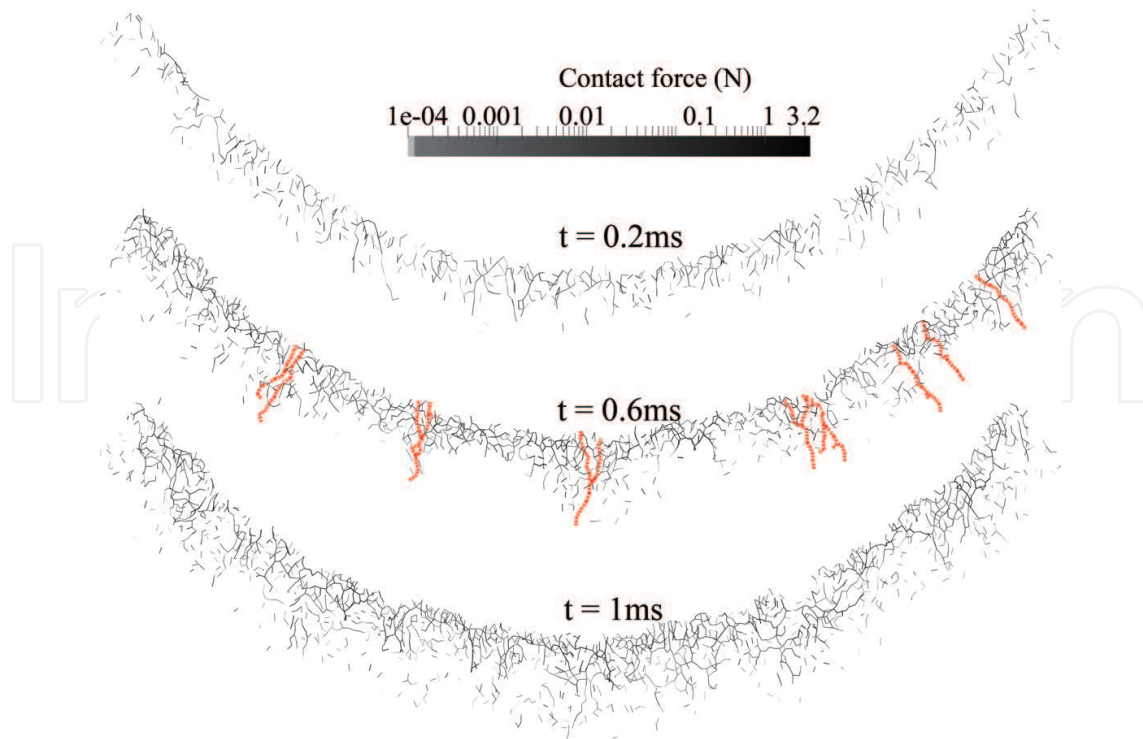


**Figure 20.** Snapshots of the network of force chains in the bottom section of the particle ring subjected to the shock loading of  $P_0 = 20$  bar in early times. Force chains (denoted by the thick dashed red lines) at  $t = 0.6$  ms indicate the long linear force chains acting as the nuclei of the force chain clustering [25].

The variations in the circumferential distributions of strong contact density,  $\rho_{\text{contact}}$ , in early times (see **Figure 21**), demonstrate how the particle-scaled heterogeneities evolve into the macroscale clusters of strong contacts indicated by the contact force peaks with width much larger than the particle size. Note that the agglomeration of force chains is well ahead of the formation of the nonuniform velocity profile that signifies the beginning of the particle clustering. Since the momentum alongside the stresses is being transmitted along the force chains, leaving the particles disconnected from the force chains, there are few chances to obtain the momentum. Particles connected by the strong force chains are supposed to move faster than those cut off from the contact network. Force chains thus act as the main channels of momentum at least in early times as suggested by the strong correlation between the Azimuthal distribution of contact density  $\rho_{\text{contact}}$  and radial velocity  $V_r$  in the first millisecond as shown in **Figure 21(a)**.

Force chains also play a major role in the elimination of weak jets caused by the dilating strong jets as demonstrated in **Figure 22**. With the incipient jets (composed of the red circles in **Figure 22**) moving ahead of the slow-moving particles (denoted by the green-dashed circles in **Figure 22**), velocity differences across the edges of the incipient jets retard any sustained contacts, leading to the weakened lateral confinement imposed on the jets. Therefore, nontrivial transverse flows occur along the edges of jet, the jet front flaring out significantly (see the middle panel in **Figure 22**). The lateral expansion of adjacent jets, especially the jet heads, squeezes the slow-moving particles in between (denoted by blue-dotted circles in **Figure 22**) establishing an intricate network of force chains therein

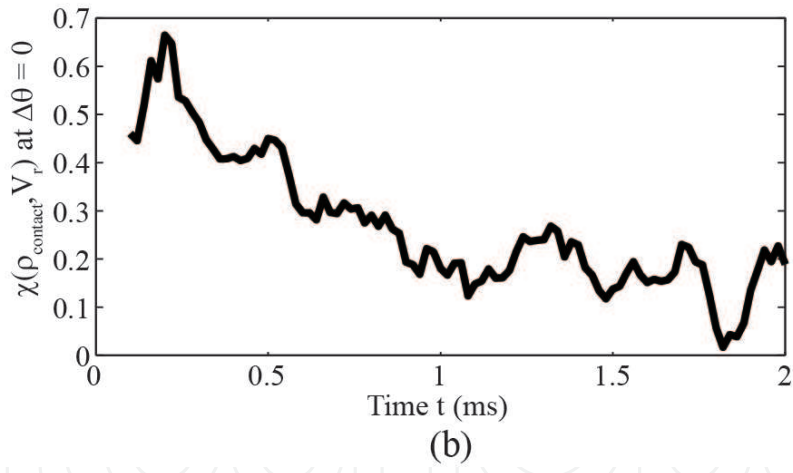
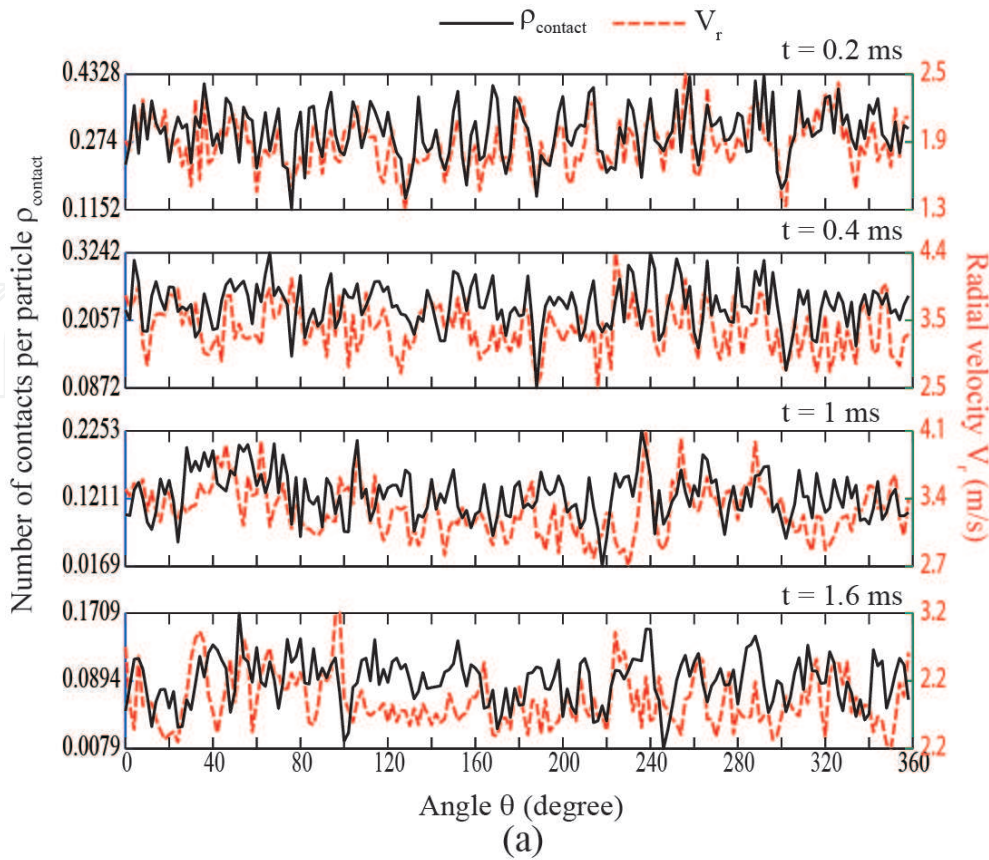


**Figure 21.** (a) Azimuthal distribution of contact density  $\rho_{\text{contact}}$  and radial velocity  $V_r$  of particle ring at different times and (b) temporal evolution of correlation coefficient between  $\rho_{\text{contact}}$  and  $V_r$ .

(see the middle and bottom panels in **Figure 22**). The newly constructed force chains with the dominant transverse orientation hinder the radial transport of the momentum that is instead channeled along the transversely aligned force chains (see the middle panel in **Figure 22**). The growth of the burgeoning minor jets between two major jets is thus likely to be suppressed or even retarded. The minor jets composed of particles indicated by the dotted circle in the middle panel of **Figure 22** are degraded to the slow-moving cluster. With the slow-moving particles increasingly lagging behind, more spaces are left outside

the edges of jets, resulting in the intensified transverse flows along the edges. By contrast, the radial compaction leads to the enhanced radial resistance restraining the radial advance of the jet front such as illustrated in the bottom panel of **Figure 22**. At some point, the transverse flows along the edges of jets are expected to overwhelm the radial propagation. The edges of major jets curl outward toward the opposite directions so that the major jet splits into several subjets (indicated by the circles in the bottom panel in **Figure 22**). The subjets with the propagation direction deviating from that of the parental jet would undergo the same development described above until they are expelled from the outer surface.

Given that the suppression of weak jets by the strong jets is mainly responsible for the decrease of jet number, the decline rate of jet number,  $V_{jet'}$  decidedly depends on the spatial density of

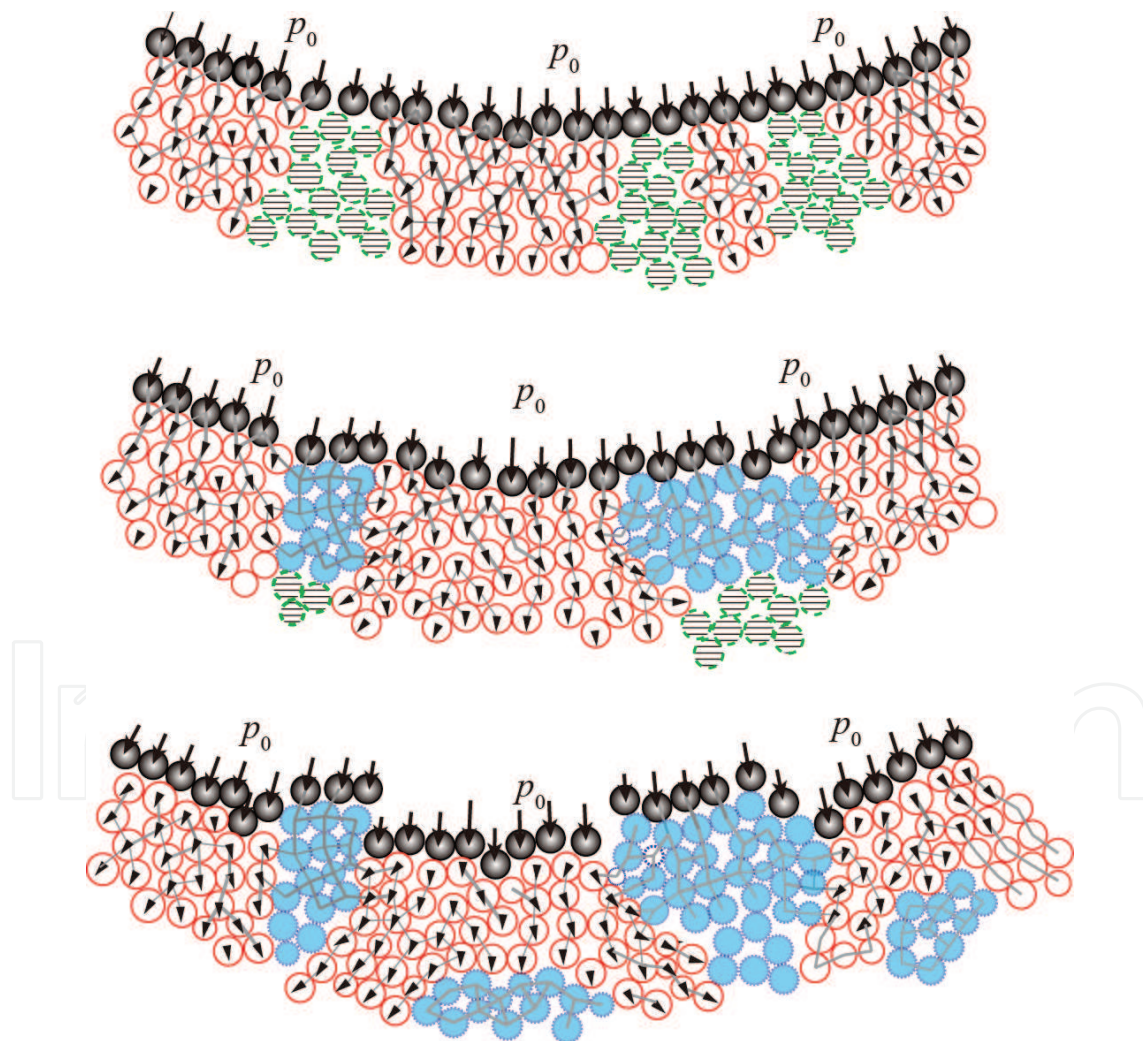


**Figure 22.** Illustrations of the evolution of the jetting pattern as well as the contact network. The red circles, dashed-line filled circles and blue filled circles represent the fast-moving particles connected by force chains, slow-moving particles without effective contacts among them, and slow-moving particles connected by transversely oriented force chains, respectively [25].

incipient jets, the perimeter of ring, and the transverse expansion of strong jets. The average spacing of initial jets varies little with  $R_{in}$  and  $p_0$ , whereas decreases with decreasing packing density and particle size. The transverse expansion of strong jets strongly correlates with the radial propagation of jets that are driven by the impulsive loadings. Accordingly, stronger shock loading intensifies both the radial and transverse expansion of jets, hastening the suppression of the adjacent weak jets.

**Figure 23** highlights the key events characterizing the formation and competitive growth of incipient jets. An excessive large number of strong force chains extruding into the bulk serves as the nuclei of incipient jets. The jets born earlier or showing stronger shear flows undergo considerable transverse flare up, annihilating the burgeoning weak jets. A substantial portion of initial incipient jets cannot survive the first instants of the phase II.

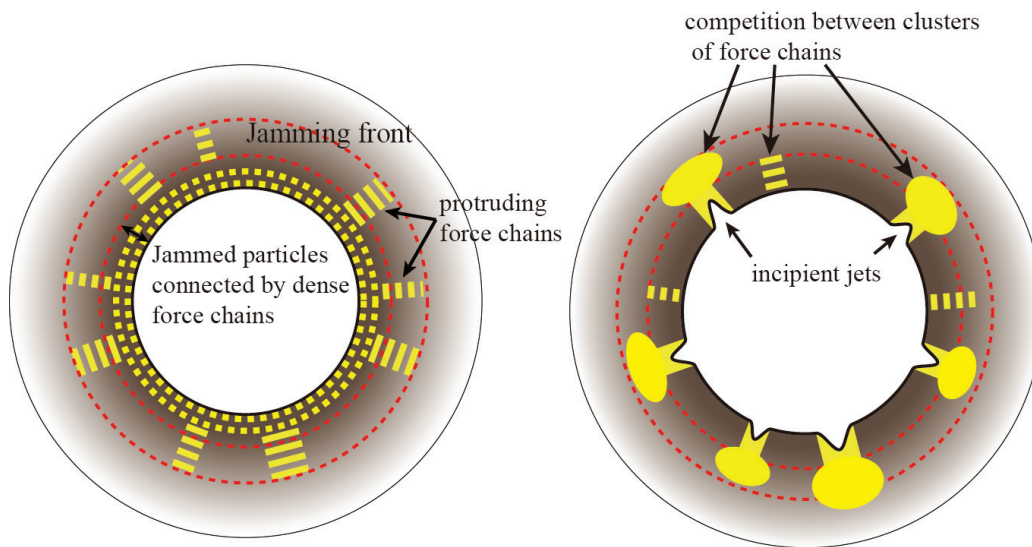


**Figure 23.** Illustration of key events dominating the formation (left) and elimination (right) of incipient jets.

#### 4. Discussion

Despite the resembling jetting pattern driven by the central explosion and radial shock loadings, the underlying mechanisms are fundamentally different as required by the distinct behaviors of particles subjected to strong blast waves and modest shock waves. In the former case, particle layers are compacted so tightly that they expand like the solids of the constituent materials. Thus, the (primary) particle jetting may well be understood from the continuum perspective since the hydrodynamic instability of interface, such as RT instability, fails to predict the jetting timescale comparable with the experimental data. Bulk fracture of compacted expanding particle layers becomes the promising candidate. The dynamic fragmentation theories of solids may well be applicable to the theoretical model of the explosion-driven particle jetting. But some major alterations need to be made to adapt these theories to the fragmentation of particle assemble. Since particles cannot sustain the tensile stresses nor have the surface energy, the fracture criterion of solids involving these two pivotal variables does

not hold in particles. Experimental results suggest that the inception of particle jetting initiates shortly after the propagation of the rarefaction wave. This observation implies that the unloading of particles triggers the particle jetting. The fractures of solids mainly nucleate at the intrinsic flaws that determine the statistics of fragment size. By contrast, the dimension of flaws in particle system, namely the inter-grain pores, contradicts with that of particle jets. It is plausible to assume that the nuclei of the particle jets may well be brought in by a strong shock interaction. The implosion of particles causes dozens of shear bands across the thickness of particle ring with attrited grains [31]. Recent experiments also collected the sintered clumps of aluminum powders after the explosive dispersal of powders [32]. The heterogeneous thermodynamic activities occurring in the blast loaded particles, such as shear banding, should be the focus of the future study. A thorough understanding in this regard needs the rigorous examination of previous experimental data and development of adequate experimental and numerical techniques providing more direct evidences.

Shock-induced particle jetting opens a fundamentally different domain but attracts relatively less attention compared with the explosion-driven particle jetting. This scenario offers an ideal opportunity to look into the transient particle flows. This chapter presents some preliminary investigations into this problem via both experimental and numerical methods. Much more work is needed to clarify the origin of the nuclei of incipient jets and the interplays between jets with varying strengths. In this regard, force chains play an essential role via introducing the inhomogeneity and modulating the jetting pattern.

## 5. Conclusion

Both explosion-driven and shock-induced particle jetting exhibit the dual jetting structure, namely, the primary jets initiating from the inner surface and the secondary jets initiating from the outer surface of particle rings/cylinders/shells. The primary and secondary jets have fundamentally different size and occur in different times so that respective mechanisms are required. More importantly, distinct behaviors of particles subjected to strong blast waves and weak shock waves dictate different mechanisms underpinning the particle jetting in both cases. Accordingly, we adopt a continuum approach to model the explosion-driven particle jetting. Specifically, a destabilization model of expanding shell is proposed to account for the onset of the primary jetting. The secondary jetting can be described by a cavitation spallation model based on the expansion of hollow spheres. The timescale and characteristic size of primary/secondary jets predicted by theoretical models agree well with the experimental data. By contrast, the shock-induced particle jetting is studied via the DEM method, which can access the particle-scale information, such as particle velocities and contact forces. The investigation reveals a two-staged evolution of particle (primary) jets, the formation and competitive growth of incipient jets. The formation of incipient jets is characterized by the transition from the homogeneous flows to the localized shear flows. The ensuing evolution of incipient jets is accompanied by the substantial annihilation of weak jets and the multiplication of strong jets. The mechanisms underlying these two phases are found to be closely related with the network of force chains.

## Author details

Kun Xue\*, Xiaoliang Shi, Kaiyuan Du and Haoran Cui

\*Address all correspondence to: xuekun@bit.edu.cn

Key State Laboratory of Explosive Science and Technology, Beijing Institute of Technology, Beijing, China

## References

- [1] Rodriguez V, Saurel R, Jourdan G, Houas L. External front instabilities induced by a shocked particle ring. *Physical Review E*. 2014;**90**:043013
- [2] Rodriguez V, Saurel R, Jourdan G, Houas L. Solid-particle jet formation under shock-wave acceleration. *Physical Review E*. 2013;**88**(6):063011
- [3] Ripley RC, Zhang F. Jetting instability mechanisms of particles from explosive dispersal. *Journal of Physics: Conference Series*. 2014;**500**(15):152012
- [4] Ripley R, Donahue L, Zhang F. Jetting instabilities of particles from explosive dispersal. *AIP Conference Proceedings*. 2011;**1426**(1):1615-1618
- [5] Milne AM, Floyd E, Longbottom AW, Taylor P. Dynamic fragmentation of powders in spherical geometry. *Shock Waves*. 2014;**24**(5):501-513
- [6] Milne A, Parrish C, Worland I. Dynamic fragmentation of blast mitigants. *Shock Waves*. 2010;**20**(1):41-51
- [7] Grégoire Y, Sturtzer M-O, Khasainov BA, Veyssi re B. Cinematographic investigations of the explosively driven dispersion and ignition of solid particles. *Shock Waves*. 2014;**24**(4):393-402
- [8] Gregoire Y, David F, Oren P. Development of instabilities in explosively dispersed particles. *AIP Conference Proceedings*. 2011;**1426**(1):1623-1626
- [9] Fue-Sang L, Tao X, Fan Z. The role of vorticity and turbulence on the instability of a dense solid particle flow. *AIP Conference Proceedings*. 2011;**1426**(1):1619-1622
- [10] Frost DL, Loiseau J, Marr BJ, Goroshin S. Particle segregation during explosive dispersal of binary particle mixtures. *AIP Conference Proceedings*. 2017;**1793**(1):120020
- [11] Frost, D.L., Gregoire, Y., Goroshin, S., and Zhang, F., "Interfacial instabilities in explosive gas-particle flows," *Proceedings of 23rd International Colloquium on the Dynamics of Explosions and Reactive Systems*, Univ. of California, Irvine, July 24-29, 2011
- [12] David LF, Yann G, Oren P, Samuel G, Fan Z. Particle jet formation during explosive dispersal of solid particles. *Physics of Fluids*. 2012;**24**(9):091109

- [13] Xue K, Li F, Bai C. Explosively driven fragmentation of granular materials. *The European Physical Journal E*. 2013;**36**(8):1-16
- [14] Zhang F, Frost DL, Thibault PA, Murray SB. Explosive dispersal of solid particles. *Shock Waves*. 2001;**10**(6):431-443
- [15] Zhang F. Metalized heterogeneous detonation and dense reactive particle flow. *AIP Conference Proceedings*. 2011;**1426**(1):27-34
- [16] Ritzel D., Ripley R., Murray S., Anderson J.: Near-field blast phenomenology of thermobaric explosions. In: Hannemann K., Seiler F. (eds) *Shock Waves*(2009);305-310. Springer, Berlin, Heidelberg
- [17] Frost DL, Ornthanalai C, Zarei Z, Tanguay V, Zhang F. Particle momentum effects from the detonation of heterogeneous explosives. *Journal of Applied Physics*. 2007;**101**(11):113529
- [18] Clark AH, Kondic L, Behringer RP. Particle scale dynamics in granular impact. *Physical Review Letters*. 2012;**109**:238302
- [19] Zhang F, Ripley RC, Yoshinaka A, Findlay CR, Anderson J, von Rosen B. Large-scale spray detonation and related particle jetting instability phenomenon. *Shock Waves*. 2015;**25**(3):239-254
- [20] Zarei Z, Frost D. Simplified modeling of blast waves from metalized heterogeneous explosives. *Shock Waves*. 2011;**21**(5):425-438
- [21] David LF, Fan Z, Susan M, Stephen BM, Andrew JH, Marta S, Marc C-C, Chayawat O. Near-field impulse effects from detonation of heterogeneous explosives. *AIP Conference Proceedings*. 2002;**620**(1):946-949
- [22] Xue K, Yu Q, Bai C. Dual fragmentation modes of the explosively dispersed granular materials. *The European Physical Journal E*. 2014;**37**:88
- [23] Xu T, Lien F-S, Ji H, Zhang F. Formation of particle jetting in a cylindrical shock tube. *Shock Waves*. 2013;**23**:619-634
- [24] Frost DL, Goroshin S, Ripley RC, Zhang F. Jet formation during explosive particle dispersal. City. 2010
- [25] Xue K, Sun L, Bai C. Formation mechanism of shock-induced particle jetting. *Physical Review E*. 2016;**94**(2):022903
- [26] Grujicic M, Pandurangan B, Qiao R, Cheeseman BA, Roy WN, Skaggs RR, Gupta R. Parameterization of the porous-material model for sand with different levels of water saturation. *Soil Dynamics and Earthquake Engineering*. 2008;**28**(1):20-35
- [27] Grujicic M, Pandurangan B, Cheeseman BA, Roy WN, Skaggs RR. Application of the modified compaction material model to soil with various degrees of water saturation. *Shock and Vibration*. 2007;**14**:1-15

- [28] Borg JP, Grady D, Cogar JR. Instability and fragmentation of expanding liquid systems. *International Journal of Impact Engineering*. 2001;**26**(1-10):65-76
- [29] Huang X, Ling Z, Dai LH. Cavitation instabilities in bulk metallic glasses. *International Journal of Solids and Structures*. 2013;**50**(9):1364-1372
- [30] Tai Q, Sadd MH. A discrete element study of the relationship of fabric to wave propagational behaviours in granular materials. *International Journal for Numerical and Analytical Methods in Geomechanics*. 1997;**21**:295-311
- [31] Nesterenko VF, Meyers MA, Chen HC. Shear localization in high-strain-rate deformation of granular alumina. *Acta Materialia*. 1996;**44**(5):2017-2026
- [32] Frost DL, Loiseau J, Goroshin S, Zhang F, Milne A, Longbottom A. Fracture of explosively compacted aluminum particles in a cylinder. *AIP Conference Proceedings*. 2017;**1793**(1): 120019